Cell

Growth of the maternal intestine during reproduction

Graphical abstract

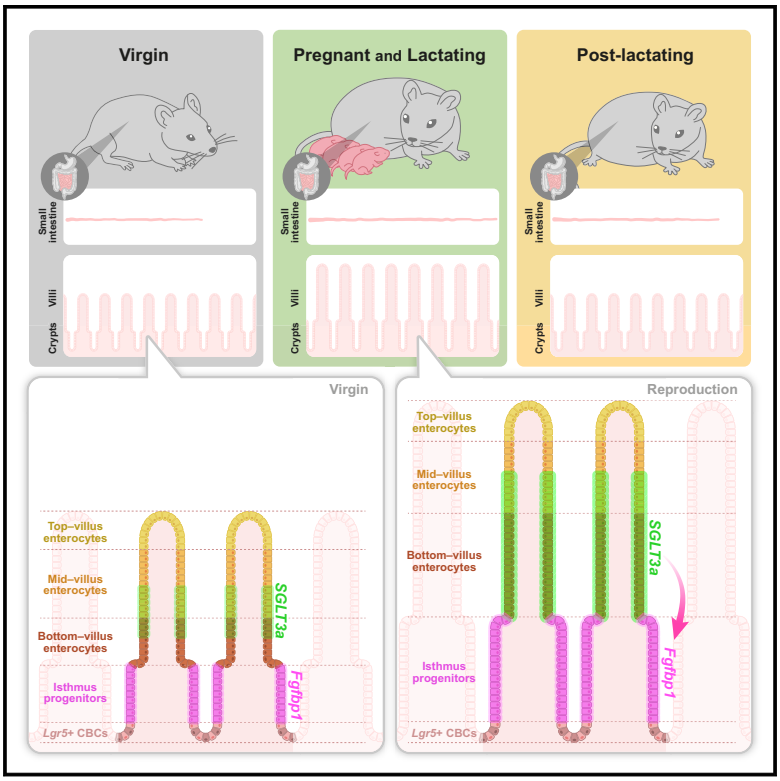

Highlights

- Resizing of the maternal intestine in pregnancy has unique and anticipatory features
- Intestinal elongation is partially irreversible, and villus growth is fully reversible
- Sodium- and proton-sensitive SGLT3a transporter is induced by pregnancy in enterocytes
- SGLT3a extrinsically sustains *Fgfbp1*+ isthmus progenitor expansion and villus growth

Authors

Tomotsune Ameku, Anna Laddach, Hannah Beckwith, ..., Vassilis Pachnis, Nicholas W. Bellono, Irene Miguel-Aliaga

Correspondence

irene.miguelaliaga@crick.ac.uk

In brief

In mice, pregnancy elongates the maternal small intestine and its villi. Reproductive remodeling is distinct from diet- or microbiota-induced changes and involves SGLT3a-driven progenitor expansion, revealing organ- and state-specific growth programs that could enhance pregnancy outcomes.

Ameku et al., 2025, Cell *188*, 2738–2756
May 15, 2025
https://doi.org/10.1016/j.cell.2025.02.015

CellPress

CellPress
OPEN ACCESS

Cell

Article

Growth of the maternal intestine during reproduction

Tomotsune Ameku,[1,2,3] Anna Laddach,[1,12] Hannah Beckwith,[2,3,12] Alexandra Milona,[1,2,3] Loranzie S. Rogers,[4] Cornelia Schwayer,[5,6] Emma Nye,[1] Iain R. Tough,[7] Jean-Louis Thoumas,[8] Umesh Kumar Gautam,[9] Yi-Fang Wang,[2] Shreya Jha,[2] Alvaro Castano-Medina,[1,3] Christopher Amourda,[1,2] Patric M. Vaelli,[4] Sira Gevers,[10] Elaine E. Irvine,[2,3] Leah Meyer,[11] Ivan Andrew,[2] Ka Lok Choi,[2] Bhavik Patel,[2] Alice J. Francis,[2] Chris Studd,[2,3] Laurence Game,[2] George Young,[2] Kevin G. Murphy,[11] Bryn Owen,[11] Dominic J. Withers,[2,3] Maria Rodriguez-Colman,[10] Helen M. Cox,[7] Prisca Liberali,[5,6] Martin Schwarzer,[9] François Leulier,[8] Vassilis Pachnis,[1] Nicholas W. Bellono,[4] and Irene Miguel-Aliaga[1,2,3,13,*]

[1]The Francis Crick Institute, 1 Midland Road, London NW1 1AT, UK
[2]MRC Laboratory of Medical Sciences, Hammersmith Hospital Campus, Du Cane Road, London W12 0NN, UK
[3]Institute of Clinical Sciences, Faculty of Medicine, Imperial College London, Du Cane Road, London W12 0NN, UK
[4]Department of Molecular and Cellular Biology, Harvard University, Cambridge, MA 02138, USA
[5]Friedrich Miescher Institute for Biomedical Research, Fabrikstrasse 24, 4056 Basel, Switzerland
[6]ETH Zürich, Department for Biosystems Science and Engineering (D-BSSE), Basel, Switzerland
[7]King's College London, Wolfson Sensory, Pain and Regeneration Centre, Hodgkin Building, Guy's Campus, London SE1 1UL, UK
[8]Institut de Génomique Fonctionnelle de Lyon, Ecole Normale Supérieure de Lyon, CNRS UMR5242, UCBL Lyon-1, 69007 Lyon, France
[9]Laboratory of Gnotobiology, Institute of Microbiology of the Czech Academy of Sciences, 54922 Novy Hradek, Czech Republic
[10]Molecular Cancer Research, Center for Molecular Medicine, University Medical Center Utrecht, 3584 CG Utrecht, the Netherlands
[11]Department of Metabolism, Digestion, and Reproduction, Faculty of Medicine, Imperial College London, Du Cane Road, London W12 0NN, UK
[12]These authors contributed equally
[13]Lead contact
*Correspondence: irene.miguelaliaga@crick.ac.uk
https://doi.org/10.1016/j.cell.2025.02.015

SUMMARY

The organs of many female animals are remodeled by reproduction. Using the mouse intestine, a striking and tractable model of organ resizing, we find that reproductive remodeling is anticipatory and distinct from diet- or microbiota-induced resizing. Reproductive remodeling involves partially irreversible elongation of the small intestine and fully reversible growth of its epithelial villi, associated with an expansion of isthmus progenitors and accelerated enterocyte migration. We identify induction of the SGLT3a transporter in a subset of enterocytes as an early reproductive hallmark. Electrophysiological and genetic interrogations indicate that SGLT3a does not sustain digestive functions or enterocyte health; rather, it detects protons and sodium to extrinsically support the expansion of adjacent Fgfbp1-positive isthmus progenitors, promoting villus growth. Our findings reveal unanticipated specificity to physiological organ remodeling. We suggest that organ- and state-specific growth programs could be leveraged to improve pregnancy outcomes or prevent maladaptive consequences of such growth.

INTRODUCTION

The intestine is a remarkably plastic organ: its epithelium is the fastest self-renewing tissue in mammals. In the small intestine, proliferating cells located within crypts give rise to cells that migrate upward into the villus and differentiate into enterocytes and secretory cell types before finally undergoing apoptosis at the villus tip.[1–5] Although the exact lineage relationship between actively cycling crypt cells remains a matter of active investigation, both Lgr5-positive crypt base columnar (CBC) cells and Fgfbp1-positive isthmus progenitors located at the base and sides of the crypt, respectively, proliferate and can give rise to multiple intestinal cell types.[6–8] Much of our understanding of the plasticity of organs such as the intestine derives from investigating responses to tissue damage, nutrient deprivation/excess, or microbiota depletion.[9] Paradoxically, we have historically overlooked one of the most physiologically relevant contexts in which adult organs grow: reproduction.

Reproductive growth of the maternal intestine and other organs was suggested nearly 100 years ago[10] and has since been shown to involve increases in intestinal length and absorptive area.[10–14] The underlying mechanisms are only beginning to be investigated,[15] and questions remain as to whether these

mechanisms are shared between organs or with other environmental triggers of intestinal remodeling.[9,16–19]

We have previously shown that remodeling of the maternal intestine is not confined to mammals. Indeed, the intestine of oviparous *Drosophila* fruit flies, which differs between males and females, grows and is metabolically remodeled in females during reproduction.[20–22] We and others showed that intestinal growth is anticipatory and genetically controlled. It requires but does not passively result from increased nutrient intake or nutritional demands during reproduction.[21–28]

These findings prompted us to revisit and functionally interrogate the reproductive growth of the mouse intestine with modern genetic tools. Here, we describe its cellular features and uncover underlying molecular changes and triggers.

RESULTS

Dynamics of intestinal elongation and villus growth during pregnancy

The small intestine of males and virgin females is comparable in length (Figure 1C), but, in keeping with previous studies,[29,30] we observed significant increases in intestinal length and mass in lactating females (Figures 1A–1C and S1I). Lengthening is already apparent on pregnancy day 7 (Figure 1C) and continues throughout pregnancy. Toward the end of pregnancy (day 18), the small intestine is circa 18% longer and comparable to that of lactating females (lactation day 7) (Figures 1B and 1D).

Elongation is only partially reversible: at 7 days and even 35 days post-lactation, the small intestine remains longer than that of virgin female mice (Figures 1B and 1D). Likely as a result of this incomplete reversal, the small intestine of lactating female mice is longer after a second pregnancy than after the first (Figure 1C; age-matched virgin females were used in both cases to control for age-related effects on gut elongation).

Histologically, crypts have deepened by the end of pregnancy, and villi have become wider and 20%–30% longer (Figures 1E–1E″, 1G, and S1A, ileum sections). Crypt and villi elongation is apparent along the entire length of the small intestine (Figures S1C–S1H; see also Mendeley Data S1). Although the dynamics of villus growth are comparable to those of gut elongation (namely, already apparent by day 7 of pregnancy and fully elongated by the end of pregnancy), they differ in their reversibility: only 7 days post-lactation, villus height, width, and crypt depth have all returned to pre-pregnancy values (Figure S1A′). Consistently (and unlike gut elongation), the reproductive expansion of villi is not cumulative: the height of villi during a second pregnancy is comparable to that during a first pregnancy (Figure 1F).

Hence, remodeling of the maternal intestine involves elongation of both the gut and its crypt/villus units. The former is cumulative and only partially reversible, whereas the latter is fully reversible. In light of the observed dynamics, we conducted subsequent investigations at pregnancy day 7 and lactation day 7 to capture earlier remodeling events and their endpoint, respectively.

Reproductive changes in epithelial cell dynamics

Changes in villus height may ensue from changes in cell size, number, or both. Changes in cell number may, in turn, be achieved by adjusting cell proliferation and/or death. We next examined contributions of these cellular features to the reproductive expansion of villi.

We first performed tracing experiments using 5-ethynyl-2′-deoxyuridine (EdU) injections, incorporated into proliferating cells and their progeny,[31] and visualized EdU incorporation and Ki67 protein (used as a marker for proliferating cells[32]) in tissue sections. Both the number of Ki67-positive proliferating cells and their newly generated progeny (calculated as the fraction of EdU-positive/proliferative Ki67-positive cells) are increased at day 7 of pregnancy and remain high at lactation day 7 (Figures 2A and 2B). In both pregnancy and lactation, proliferating Ki67-positive cells were particularly apparent in the crypt isthmus, which harbors Fgfbp1-positive intestinal progenitors (previously referred to as transit-amplifying cells).[7,8,33] Of note, the sustained proliferation increase observed in lactation contrasts with the recently described pregnancy-responsive activation of neural stem cells, which does not extend beyond pregnancy and gives rise to short-lived neurons.[34] We also observed accelerated migration of the enterocyte progeny up the villus in early pregnancy and, particularly, in lactation (Figures 2A and 2B). Indeed, while EdU-labeled enterocytes had migrated about one-third of the total crypt-villus length following a 24 h EdU pulse in virgin females (consistent with previous evidence that it takes newly generated cells 3–5 days to reach the top of the villus[5]), they were found close to the tip of the villus in lactating mice (Figures 2A and 2B), suggesting that it takes them just over a day (1.3 days) to reach the top of the villus at this stage. Only 7 days after weaning, the rates of both progenitor proliferation and enterocyte migration have fully returned to pre-pregnancy rates, in line with the full reversibility of anatomical crypt-villus features (Figures 2C and 2D).

We next conducted semi-automated quantifications of sections labeled with terminal deoxynucleotidyl transferase dUTP nick end labeling (TUNEL) and the apoptosis marker cleaved caspase-3 (CC3) (see STAR Methods for details).[35–37] In virgin female mice, we observed apoptotic cells in the tip of the villus (where cell extrusion is known to occur[38]) and, sporadically, in the mid/bottom-villus region and in crypts (Figure S1B; Table S1). In pregnant and lactating animals, the number of apoptotic cells was either unchanged or, in the case of the mid/bottom-villus region, increased depending on the marker used to assess cell death. The increased proportion of apoptotic cells in this region had returned to virgin levels 7 days post-lactation (Table S1). These findings suggest that epithelial expansion during reproduction is not caused by reduced cell death.

Finally, using semi-automated area quantifications of cells within villi (Figure 2E; see STAR Methods for details), we observed increased size of differentiated epithelial cells within villi in both pregnant and lactating mice (Figure 2F). Again, this effect was reversible (Figure 2G).

Hence, villi grow during pregnancy by increasing the proliferation of their progenitors and the migration and size of differentiated epithelial cells. Consistent with the dynamics of villus growth/shrinkage, these reproductive changes in epithelial cell dynamics are already apparent in early pregnancy, peak at the end of pregnancy, persist in lactation, and yet are fully and rapidly reversible post-lactation.

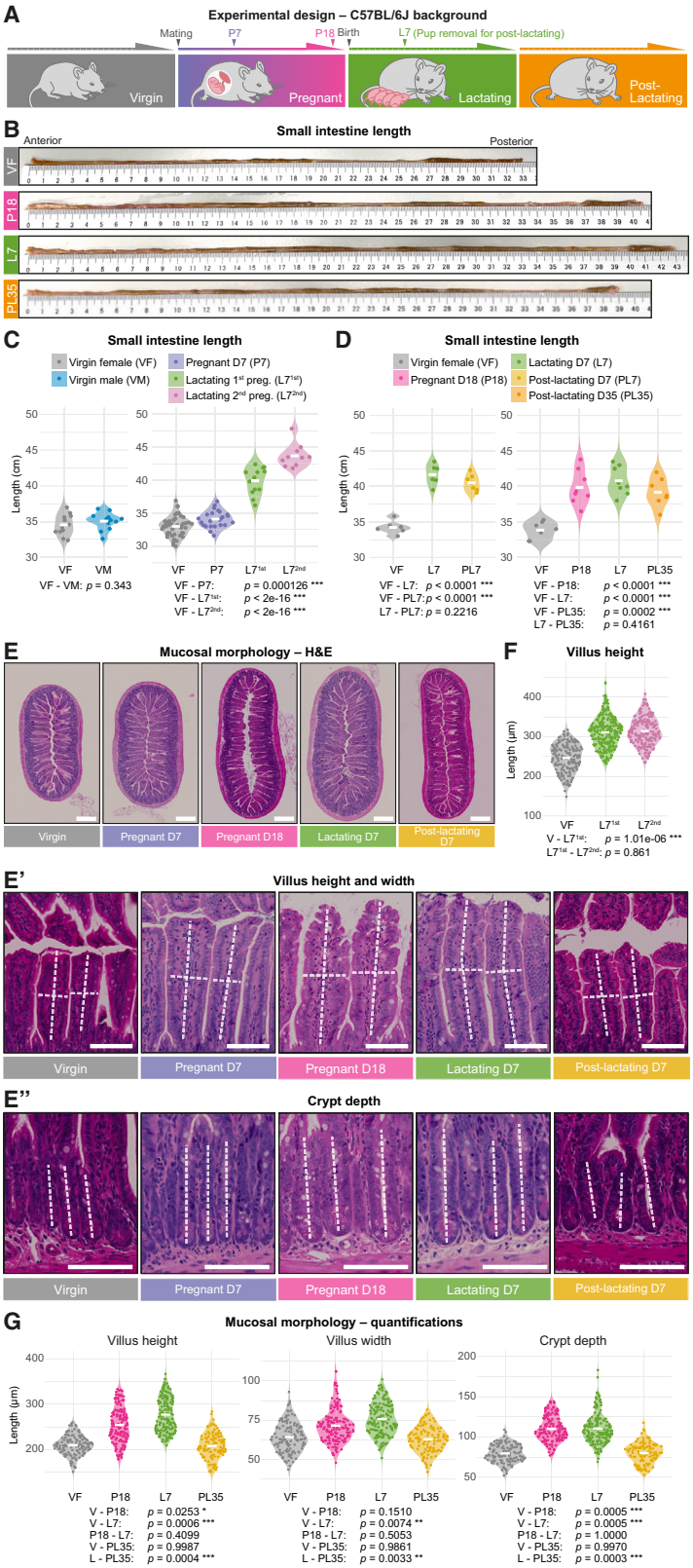

Figure 1. Dynamics and reversibility of gut and villi elongation during pregnancy

(A) Summary of experimental design.

(B) Representative images of small intestine from virgin female (VF), pregnant day 18 (P18), lactating day 7 (L7), and post-lactating day 35 (PL35).

(C) Small intestinal length of VF ($n = 41$), virgin male (VM, $n = 35$) (left), VF ($n = 46$), P7 ($n = 24$), and L7 ($L7^{1st}$ or $L7^{2nd}$, post-1^{st} or 2^{nd} pregnancy, $n = 13$ and 10, respectively) mice (right).

(D) Small intestinal lengths of VF ($n = 6$), L7 ($n = 6$), and PL7 ($n = 7$) (left) and VF ($n = 7$), P18 ($n = 8$), L7 ($n = 8$), and PL35 ($n = 7$) mice (right).

(E–E″) Representative H&E images of ileal cross-section (E), villus height and width (E′), and crypt depth (E″). Scale bars, 300 µm (E) and 100 µm (E′ and E″).

(F and G) Morphometric quantifications of ileal villus height of VF ($n = 9$), L7 ($L7^{1st}$ and $L7^{2nd}$, post-1^{st} or 2^{nd} pregnancy, $n = 16$ and 9, respectively) (F), and ileal villus height, villus width, and crypt depth of VF ($n = 7$), P18 ($n = 8$), L7 ($n = 8$), and PL35 ($n = 7$) mice (G). Original sections analyzed in (F) are also shown in Figures 7E and S1H.

p values are estimated using a linear mixed-effects model (lme4 and lmerTest R package; see STAR Methods for details) with a two-sample test in (C), (F), and (G) and a one-way ANOVA with Tukey's multiple comparisons test in (D). In all quantifications, $*p < 0.05$, $**p < 0.01$, $***p < 0.001$.

See also Figure S1 and Table S1.

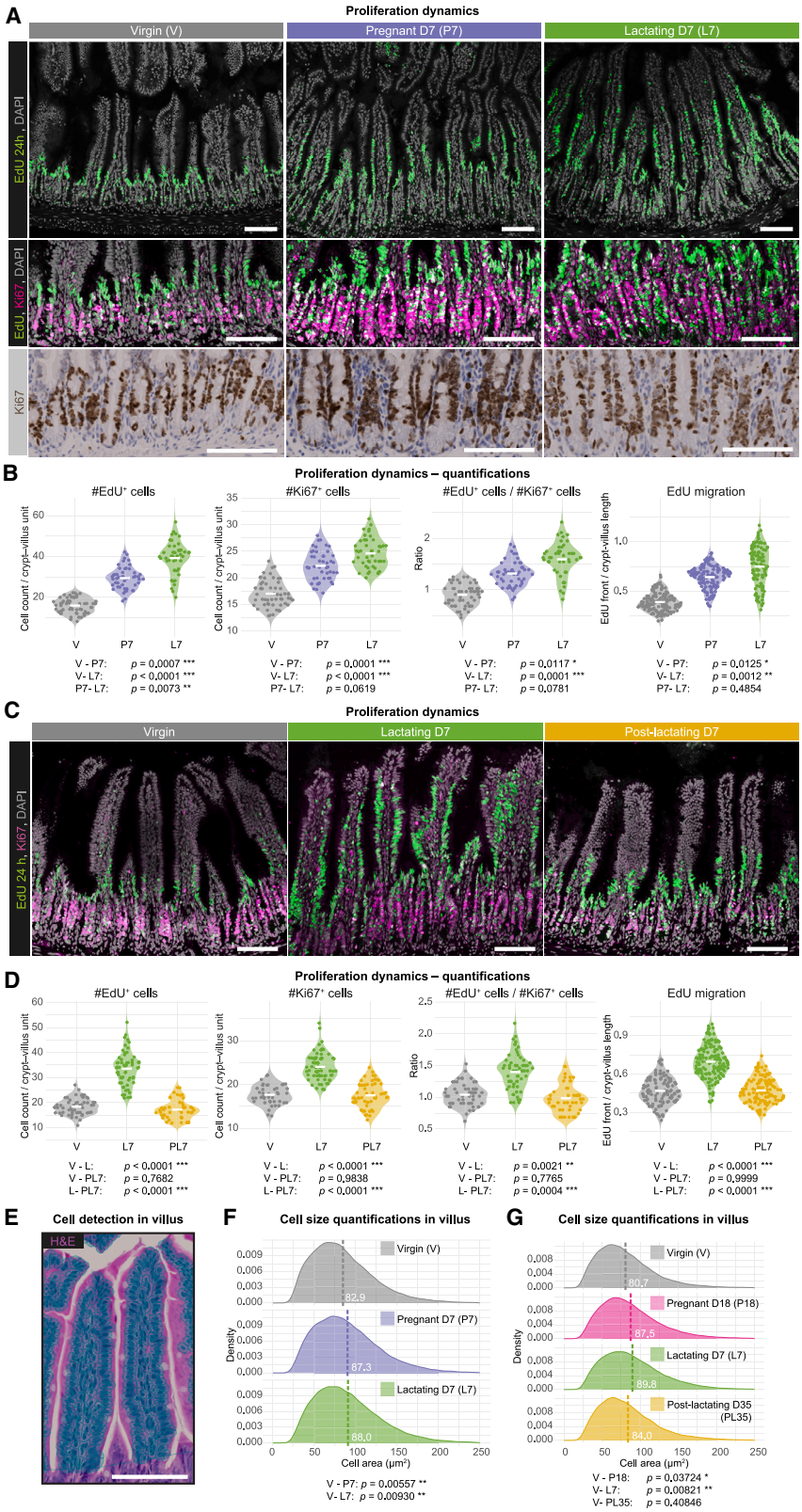

Figure 2. Reproductive changes in epithelial cell dynamics

(A and C) Representative images of EdU and anti-Ki67 staining in the ileum of virgin (V), P7, and L7 mice (A) and V, L7, and PL7 mice (C). EdU pulse was introduced by intraperitoneal (i.p.) injection, and the gut tissues were harvested 24 h after injection. Scale bars, 100 μm.

(B and D) Quantifications of proliferation dynamics in the ileum of V (n = 6), P7 (n = 6), and L7 (n = 6) mice (B), and V (n = 6), L7 (n = 8), and PL7 (n = 6) mice (D). See STAR Methods for details.

(E) Representative H&E image of villus cell detection by QuPath (see STAR Methods for details). Scale bar, 100 μm.

(F and G) Quantifications of villus cell size in the ileum of V (n = 12), P7 (n = 15), and L7 (n = 10) mice (F), and V (n = 7), P18 (n = 8), L7 (n = 8), and PL35 (n = 7) mice (G).

p values are estimated using a linear mixed-effects model (lme4 and lmerTest R package; see STAR Methods for details) with a two-sample test in (B), (D), (F), and (G). In all quantifications, $^{*}p < 0.05$, $^{**}p < 0.01$, $^{***}p < 0.001$.

See also Figure S1 and Table S1.

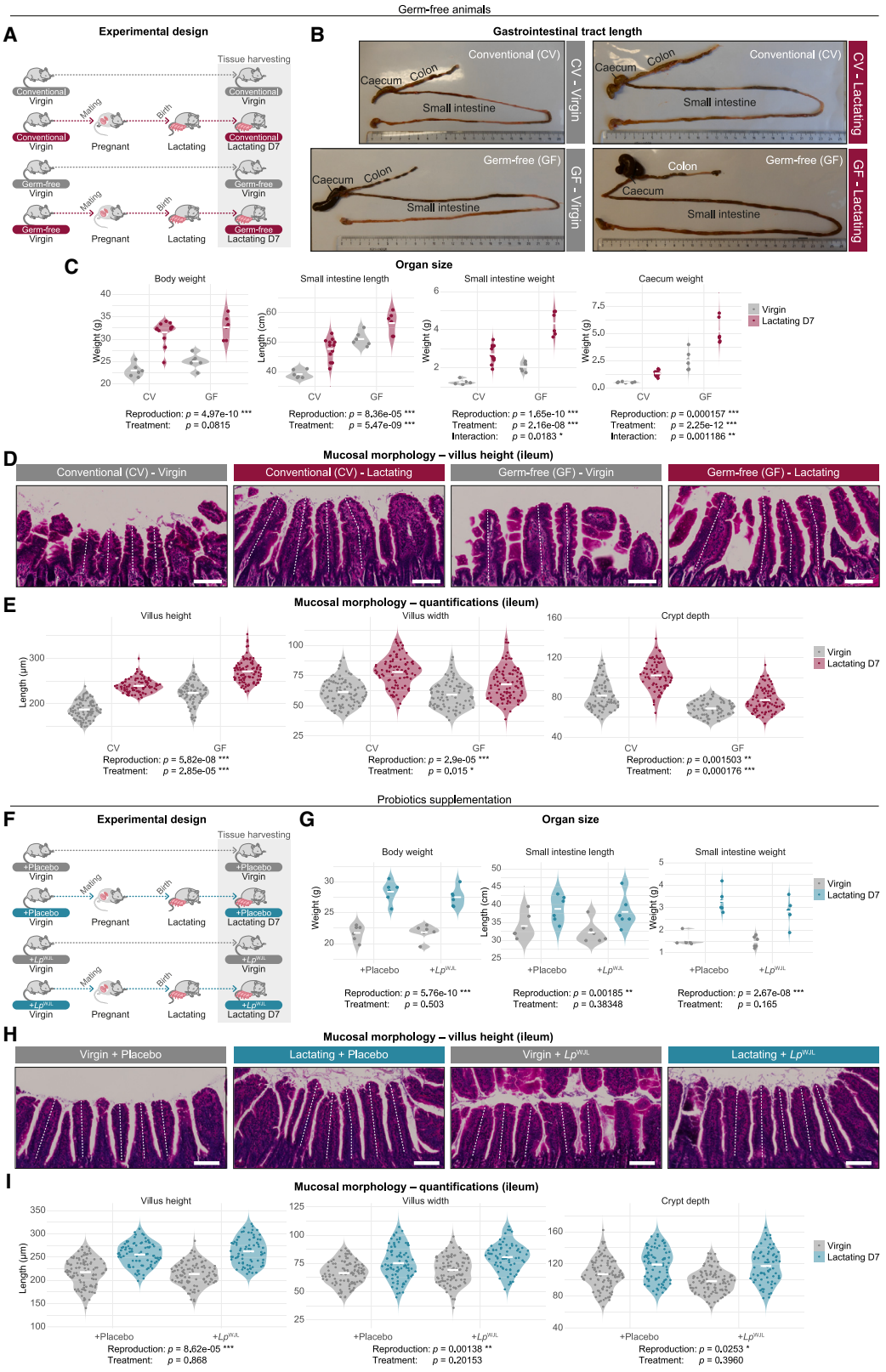

(legend on next page)

Reproductive remodeling of the intestine precedes and can be uncoupled from other reproductive adaptations

Food intake is a positive determinant of intestinal surface area.[9,39] Is the growth of the maternal intestine secondary to the increased food intake of pregnant and lactating females? Both the food intake and body weight of female mice increase during pregnancy and lactation (Figures S1J–S1L), and reproductive intestinal growth does, to some extent, require hyperphagia.[12,14,40] However, intestinal elongation and mucosal remodeling (already apparent at pregnancy day 7) precede the reproductive increase in daily food intake,[41,42] which does not become significant until day 12 or 13 depending on the quantification method used (Figures S1K and S1L; see also Mendeley Data S2).

Pregnancy also alters the gut microbiome.[43] Because the intestine of germ-free mice is longer,[17,44] we wondered whether reproductive remodeling might result from pregnancy-associated changes in microbial load and/or composition. We first assessed reproductive adaptations in gnotobiotic females born and raised in sterile conditions (Figure 3A). The weight of these females is comparable to conventionally reared females prior to pregnancy, and weight has also increased to a comparable degree at lactation day 7 in these females (Figure 3C). As previously reported,[44] the small intestine of germ-free virgin female mice is longer, and their cecum is larger (Figures 3B and 3C). However, the small intestine of these mice still elongates during reproduction by a fraction comparable to that of conventionally reared mice (Figures 3B and 3C). Similarly, while morphological crypt-villus features are all affected in germ-free virgin female mice (notably, villi are already longer), crypt-villus units undergo comparable reproductive changes to those of conventionally reared female mice (Figures 3D and 3E). Hence, the maternal intestine is still remodeled by reproduction in the absence of microbiota. In parallel, we tested the possibility that reproductive remodeling results from a bacterial deficit during pregnancy.[17,43] If this was the case, probiotic supplementation during pregnancy may blunt intestinal resizing. To test this, we supplemented the diet of females throughout pregnancy and lactation with *Lactiplantibacillus plantarum* (WJL strain). This particular strain has previously been shown to rescue the blunted growth of undernourished infant mice and modulate intestinal stem cell proliferation (Figure 3F).[45–47] The weight and length of small intestine of *L. plantarum*^{WJL}-treated females was indistinguishable from that of females treated with a placebo (see STAR Methods for details) both before and after pregnancy (Figure 3G), and pregnancy still triggered intestinal elongation and growth of both villi and crypts (Figures 3G–3I).

Together, these experiments suggest that remodeling is specific to reproductive status, rather than passively resulting from microbial changes or increased food intake.

Transcriptional and spatial changes in the small intestine during reproduction

To characterize reproductive changes molecularly, we first conducted bulk RNA sequencing (RNA-seq). Consistent with our anatomical analyses, transcriptional differences were more pronounced within females depending on their reproductive status than between virgin females and males (Table S2; see also Mendeley Data S3). Reproductive changes were apparent in duodenal, jejunal, and ileal regions and included genes encoding proteins involved in metabolism, signaling, and immunity, suggestive of changes in multiple cell types (Table S2; see also Mendeley Data S3).

We next focused on the ileum because it underwent more extensive transcriptional remodeling (Table S2) and performed single-cell RNA-seq (scRNA-seq) of fluorescence-activated cell sorting (FACS)-sorted intestinal epithelial cells (54,493 cells; Table S3; see also Mendeley Data S4) to identify epithelial changes. We conducted unsupervised graph-based clustering and cell-type annotation based on known marker genes[48,49] (Table S3; see also Mendeley Data S4) for *Lgr5*-positive crypt base columnar (CBC), isthmus progenitor, Paneth, goblet, enteroendocrine (EE), and top-, mid-, and bottom-villus enterocyte clusters (Figures 4A and 4D; see STAR Methods for details).

Pseudobulk differential expression (DE) analysis of each cluster revealed that reproductive remodeling was more substantial in enterocytes and differed depending on the position of these enterocytes within the villus (Figure 4B; Table S3; see also Mendeley Data S4). Gene Ontology (GO) analysis identified metabolic pathways among the most reproduction-regulated (Figure 4C; see also Mendeley Data S4). In enterocytes from lactating mice, we observed upregulation of genes encoding proteins involved in fatty acid handling and oxidation (*Fabp1*, *Fabp2*, and *Acaab1b*), lipid transport (*Apoa4*, *Apoc2*, *Apoc3*, *Apol9a*, and *Apol9a*), acyl-coenzyme A (CoA) metabolism (*Acsl1*, *Acsl5*, *Acot6*, *Acot7*, and *Acot12*), pyruvate metabolism (*Pdk4*), bile acid transport (*OSTβ*), sugar transport and metabolism (*SGLT1*, *GLUT2*, *Pfkfb3*, and *Pck1*), and micronutrient absorption/transport (calcium: *S100g*, zinc: *Slc39a4* and *Slc30a1*, copper: *Slc31a1*, and manganese: *Slc30a10*; Table S3). In the

Figure 3. Microbiota-independent regulation of the maternal gut growth during reproduction

(A) Summary of experimental design.

(B) Representative images of gastrointestinal tracts from V conventional (CV), lactating (L) CV, V germ-free (GF), and L GF female mice.

(C) Body weight and organ quantifications of V and L CV and GF mice (V CV, $n = 6$; L CV, $n = 12$; V GF, $n = 6$; and L GF mice, $n = 6$).

(D and E) Representative H&E images of ileal villus height (D) and morphometric quantifications of ileal villus height, width, and crypt depth (E) of V CV, L CV, V GF, and L GF mice ($n = 6$ for each group). Scale bars, 100 μm.

(F) Summary of experimental design. V and L mice were assigned to probiotics supplementation (*Lactiplantibacillus plantarum*^{WJL} strain, +*Lp*^{WJL}) or placebo control groups.

(G) Body weight and organ sizes of V and L control and treatment groups ($n = 6$ for each group).

(H and I) Representative H&E images of ileal villus height (H) and morphometric quantifications of ileal villus height, width, and crypt depth (I) of V + placebo ($n = 6$), L + placebo ($n = 6$), V + *Lp*^{WJL} ($n = 6$), and L + *Lp*^{WJL} ($n = 4$). Scale bars, 100 μm.

p values are estimated using a two-way ANOVA in (C) and (G) and a linear mixed-effects model (lme4 and lmerTest R package; see STAR Methods for details) with a two-sample test in (E) and (I).

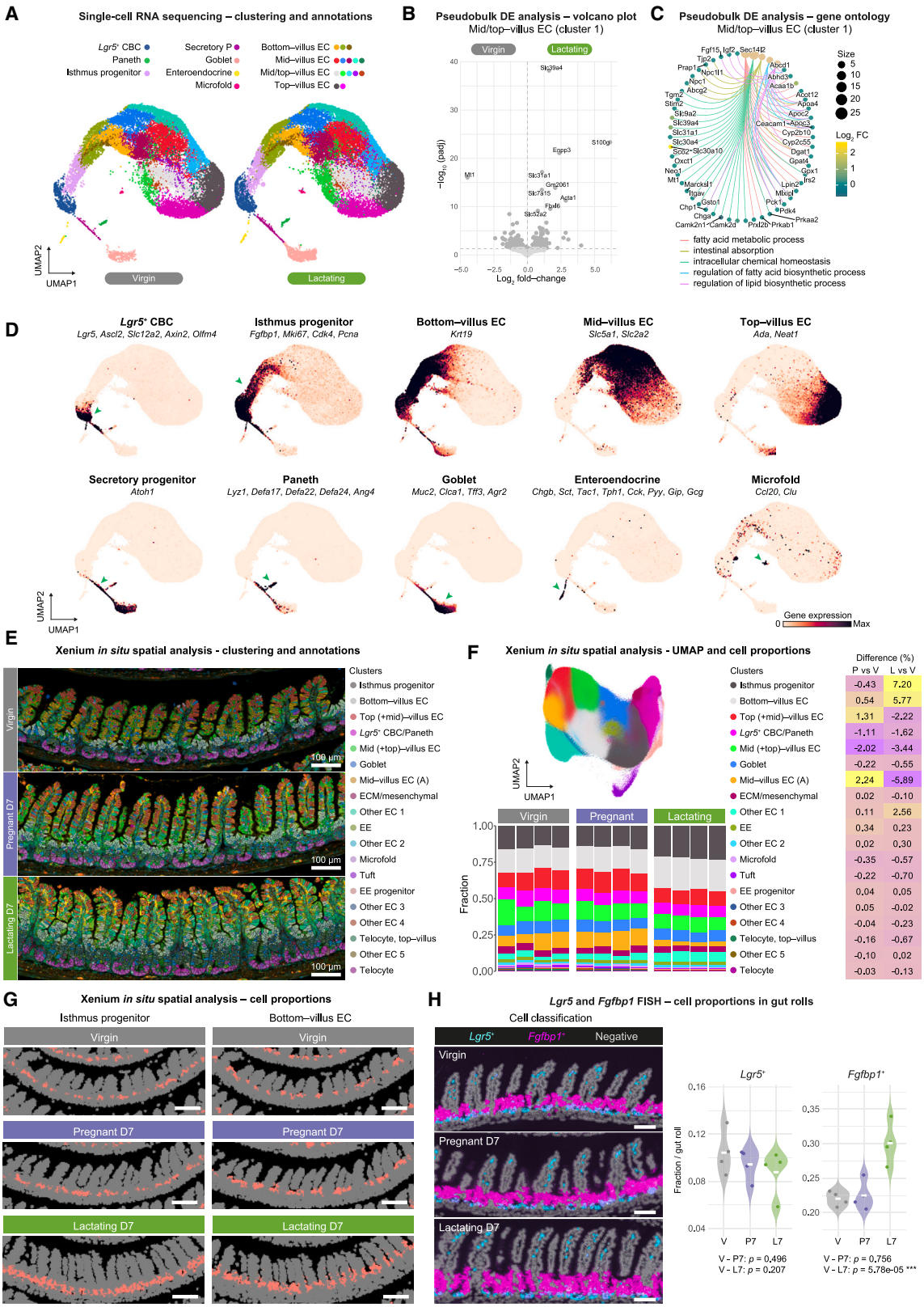

(legend on next page)

Lgr5^{+} CBC and isthmus progenitor clusters, we found upregulation of genes that are related to absorption/transport of micronutrients/metabolites (zinc: *Slc39a4*, copper: *Slc31a1*, and manganese: *Slc30a10*; Table S3).

Finally, to gain spatiotemporal insight, we conducted high-resolution spatial imaging using the Xenium *in situ* platform (see Table S4 and STAR Methods for details). As well as virgin and lactating samples, we included pregnancy day 7 samples to capture an earlier remodeling stage as well as its endpoint. We included whole ileums to provide regional information and 4 intestines per condition to control for individual variability (Figure S2A). We profiled ca. 3.5 million cells, allowing us to examine less abundant cells: EE, goblet, Paneth, and tuft cells (as well as non-epithelial cells) (Figures S2B–S2C′; Table S4). We confirmed many of the genes with reproduction-sensitive gene expression observed in our single-cell analysis and revealed additional genes with reproduction-sensitive expression in rarer cell populations—e.g., reproductive upregulation of *Cck*, *Ghrl*, and *Gcg* genes in EE cells in lactation (Figures S2D and S2D′). In terms of cell-type abundance, we observed a reproductive expansion in both the number and fraction of *Mki67*-positive isthmus progenitors and *Car4*-positive bottom-villus enterocytes per villus (with a concomitant reduction in the fraction of mid- and top-villus enterocytes, *Slc2a2*- and *Ada*-positive, respectively) in lactation (Figures 4E–4G, S2E, and S2F; Table S4). Of note, multimodal cell segmentations from the Xenium platform confirm that the reproductive increase in cell size we had observed in our whole villus segmentations (Figures 2E–2G) is apparent in these bottom-villus and mid-villus enterocyte clusters, among others (Figure S2I). We also note a relative depletion of bottom crypt (*Lgr5*-positive and Paneth) cells, whose number remains comparable during pregnancy and lactation despite the expansion of the crypt-villus unit, and a slightly (but significantly) increased fraction of EE cells in pregnancy (Figures 4E and 4F; Table S4).

To validate these findings, we conducted single-molecule fluorescence *in situ* hybridization (smFISH) of ileum cross sections and gut rolls. We used probes against *Lgr5*-positive CBCs and *Fgfbp1*-positive isthmus progenitors, as well as markers of crypt-villus axis regional identity: *Ada* for the top villus, *Slc2a2* for the mid villus, and *Krt19* for the bottom enterocyte/isthmus identity.[49] This confirmed that, during reproduction, the fractions of bottom-villus enterocytes and isthmus progenitors expand at the expense of top-villus enterocytes (Figures S2G and S2G′), the number of *Lgr5*-positive crypt cells remains constant, and there is an expansion in absolute (pregnancy day 7 and lactation day 7) and relative (lactation day 7) numbers of *Fgfbp1*-positive cells per cross section during reproduction (*Fgfbp1* expression levels within them remain comparable; Figures 4H, S2H, and S2H′; data not shown).

In sum, reproduction greatly enhances the transcriptional differences between male and female intestines. Pregnancy and lactation are associated with an increased number of isthmus progenitors and an expansion in the fraction of bottom-villus enterocytes relative to top- and mid-villus enterocytes. Within different cell types, metabolic pathways are among those most regulated by reproduction.

SGLT3a transporter expression is upregulated in a subset of enterocytes during pregnancy and lactation

To identify candidate factors driving (rather than resulting from) the reproductive remodeling of the intestinal epithelium, we compared the above datasets to a fourth bulk RNA-seq dataset of FACS-sorted intestinal epithelia at two different time points: lactation and pregnancy day 7, a time when food intake has not yet significantly increased (Figures S1K and S1L). Intersectional analysis identified *Slc5a4a* as upregulated by pregnancy and lactation across all datasets (Figures 5A and 5B; Table S5).

Slc5a4a codes for SGLT3a: a member of the sodium-glucose cotransporter (SGLT) family and one of two paralogous proteins in mice (SGLT3a and SGLT3b, encoded by *Slc5a4a* and *Slc5a4b*, respectively). Quantitative reverse-transcription PCR (RT-qPCR) revealed higher transcript levels in virgin females compared with virgin males (Figure 5C), confirmed upregulation of *Slc5a4a* (but not *Slc5a4b*) in the ileum as well as other small intestinal regions of females during pregnancy and lactation, and further revealed its rapid and fully reversible return to pre-pregnancy levels post-lactation (Figures 5C and 5D).

Consistent with the previous study by Soták et al.[50] and our transcriptomics, smFISH detected *Slc5a4a* expression in bottom- and mid-villus enterocytes (Figures 5E and 5F). Both smFISH and spatial imaging data reveal an increased number of *Slc5a4a*-expressing enterocytes within these clusters, as

Figure 4. Transcriptional and spatial characterization of maternal gut growth during reproduction

(A) Uniform manifold approximation and projection (UMAP) visualization of unsupervised clustering of 22 distinct ileum epithelial clusters (20,744 cells from 3 VF mice, 33,749 cells from 5 L female mice).

(B) Volcano plot showing DE genes between L and V samples (false discovery rate [FDR] < 0.05, above dotted horizontal line) in the mid/top-villus EC (cluster 1).

(C) Network plot of top 5 enrichment terms for DE genes identified by pseudobulk DE analysis between L and V samples in mid/top-villus EC (cluster 1).

(D) Average expression of well-established cell-type markers visualized on UMAP plots.

(E) Representative clustering and annotation of cells in the ileum of V, P7, and L7 mouse obtained by Xenium *in situ* spatial analysis (see STAR Methods for details). Scale bars, 100 μm.

(F) UMAP visualization of unsupervised clustering of 1,979,657 intestinal epithelial cells (19 clusters) identified in the ileal gut rolls of V, pregnant (P), and L female mice ($n = 4$ each) (top left). Stacked bar plots showing epithelial cell proportions in the ileal gut rolls of V, P, and L samples (bottom left). The differences (%) in each cluster between pregnant and virgin (P vs. V) and lactating and virgin (L vs. V) are shown (right). See Table S4 for full results and statistics.

(G) Spatial localization of isthmus progenitor (left) and bottom-villus EC (right) populations in V, P7, and L7 mice. Scale bars, 200 μm.

(H) FISH images showing cell classifications (*Lgr5*+ cell in cyan; *Fgfbp1*+ cell in magenta, and double-negative cell in gray) in ileal gut rolls (left) and quantifications of *Lgr5*+ and *Fgfbp1*+ cell proportions in the gut roll of V, P7, and L7 mice ($n = 4$ each) (right). Scale bars, 100 μm.

CBC, crypt base columnar; EC, enterocyte; P, progenitor; EE, enteroendocrine; A, anterior.

p values are estimated using the propeller method (speckle R package; see STAR Methods for details) in (F) and (H). In all quantifications, $^{*}p < 0.05$, $^{**}p < 0.01$, $^{***}p < 0.001$.

See also Figure S2 and Tables S2, S3, and S4.

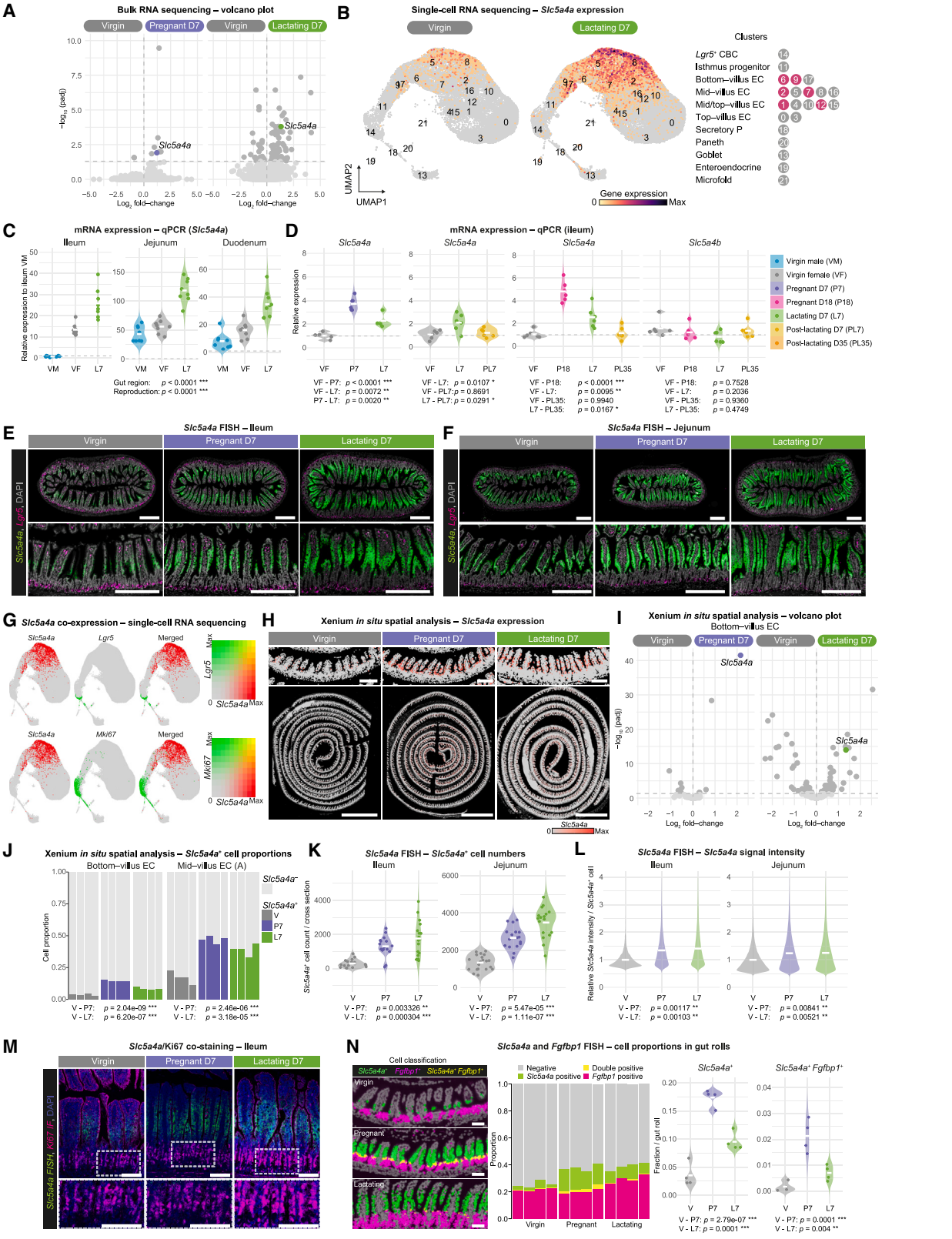

(legend on next page)

well as increased expression of *Slc5a4a* within *Slc5a4a*-expressing cells (Figures 5H–5L) during pregnancy and lactation. Single-cell data and co-staining with proliferative cell markers concur that there is no overlap between *Slc5a4a*-positive cells and *Lgr5*-positive CBCs or, more generally, Ki67-positive cells in either virgin, pregnant, or lactating guts (Figures 5G and 5M). *Slc5a4a* enterocytes are adjacent to the *Fgfbp1*-positive isthmus progenitors. Expression of these two markers is largely non-overlapping, except for a small fraction of cells at pregnancy day 7 (and to a lesser extent lactation day 7; Figure 5N). These cells are, however, not positive for proliferation markers (Figure 5M) and likely correspond to differentiating enterocytes.

SGLT3a mutation does not impair broad digestive functions but sustains reproductive metabolic plasticity within enterocytes

SGLT transporters are responsible for the active transport of glucose across membranes: they have key roles in glucose control and, in the case of SGLT1, intestinal glucose absorption from the lumen.[51] To explore possible such roles, we initially examined transgenic mice lacking both SGLT3 proteins (hereafter referred to as SGLT3^{KO}), and we subsequently validated relevant phenotypes and explored them further using mutant mice lacking SGLT3a only. SGLT3^{KO} female mice displayed no overt phenotypes: their food intake, weight, body composition, and glucose tolerance are comparable to those of control littermates both prior to and during pregnancy and lactation (Figures S3A–S3F and S5D; we note that SGLT3^{KO} but not SGLT3a^{KO} mice failed to increase body weight to the levels normally observed in lactating mice). Their intestinal physiology was also comparable: Ussing chamber measurements of epithelial functions indicate that trans-epithelial ion transport and resistance are comparable to those of control female mice, regardless of reproductive status (Figure S3G). Digestive efficiency also remains comparable between mutant and control females (Figures S3H and S3H′; we note that, even in wild-type mice, reproduction is associated with reduced digestive efficiency, somewhat unexpectedly given their longer intestine).

To explore SGLT3a roles agnostically, we performed scRNA-seq of FACS-sorted epithelial cells. We compared cells of lactating SGLT3a^{KO} female mice vs. female littermates since maternal gut growth has peaked at this stage. We profiled 48,882 cells and annotated cell types as previously (Figure S4A; Table S6). Pseudobulk DE analysis confirmed the lack of *Slc5a4a* in SGLT3a^{KO} mice and revealed transcriptional differences resulting from its absence in most clusters, particularly in the enterocyte subsets that normally upregulate SGLT3a during reproduction (hereafter referred to as SGLT3a clusters; Figures S4B–S4D). Within SGLT3a clusters, some genes/categories impacted by lactation were also affected by the SGLT3a mutation in the opposite direction (Figure S4E; Table S6), pointing to SGLT3a as an important mediator of metabolic changes associated with lactation. A case in point is ion transport: we observed changes in genes belonging to the solute carrier (SLC) family, some coding for sodium- or proton-coupled transporters (Table S6). Lactating SGLT3a^{KO} mice also showed downregulation of genes encoding proteins involved in pH regulation, such as sodium bicarbonate cotransporter (*NBC*) and extracellular carbonic anhydrases (*Car4* and *Car9*) (Table S6), proteins that regulate bile acid transport (*ASBT*, *OST*α, and *OST*β), cholesterol synthesis (*Hmgcs1*, *Hmgcr*, *Msmo1*, *Mvk*, *Pmvk*, *Mvd*, *Idi1*, *Fdps*, and *Sqle*), and long-chain fatty acid synthesis (*Elovl6* and *Elovl7*) (Figure S4F; Table S6). SGLT3a^{KO} females also displayed differences in the expression of genes involved in carbohydrate metabolism: reduced expression of genes encoding glycolytic proteins (*Pfkp*, *Pkm*, *Aldoa*, and *Pgk1*) and lactate metabolism/transport proteins (*Ldha* and *MCT4*), and concurrent upregulation of genes encoding proteins involved in glucose uptake (*SGLT1* and *GLUT2*),

Figure 5. *SGLT3a* expression is upregulated in a subset of enterocytes during pregnancy and lactation

(A) Volcano plots showing DE genes (FDR < 0.05, above dotted horizontal line) between P7 and V (left) or L and V (right) samples. *Slc5a4a* is labeled.

(B) Feature plots showing *Slc5a4a* expression on the UMAP plot in V vs. L samples. Clusters where *Slc5a4a* is differentially expressed are highlighted in magenta (right).

(C) RT-qPCR quantifications of *Slc5a4a* expression in duodenum, jejunum, and ileum of VM (n = 8), VF (n = 8), and L (n = 8–9) mice.

(D) RT-qPCR analysis of *Slc5a4a* and *Slc5a4b* expression in ileums of VF (n = 5), P7 (n = 6), and L7 (n = 4) females; VF (n = 6), L7 (n = 6), and PL7 (n = 6) females; VF (n = 6), P18 (n = 6), and L7 (n = 6); and PL35 females (n = 6).

(E and F) FISH images (*Slc5a4*a in green; *Lgr5* in magenta) in ileum (E) and jejunum (F) cross sections of V, P7, and L7 female mice. Scale bars, 300 m.

(G) Feature plots showing no expression overlap between *Slc5a4a* and *Lgr5* or *Ki67* on the scRNA-seq UMAP plot (V and L samples combined).

(H) Spatial localization of *Slc5a4a* in V, P7, and L7 female mice. Scale bars, 200 and 2,000 μm, top and bottom, respectively.

(I) Volcano plots showing DE genes (FDR < 0.05, above the dotted horizontal line) in bottom-villus EC between P and V (left) or L and V (right) samples; *Slc5a4a* is labeled.

(J) Stacked bar plots showing *Slc5a4a*-positive or negative cell proportions in bottom-villus EC (right) and anterior mid-villus EC (left).

(K and L) Number of *Slc5a4a*+ cell per cross sections (K) and *Slc5a4a* signal intensity within *Slc5a4a*+ cells in ileum and jejunum of V (n = 10), P7 (n = 9), and L7 (n = 11) female mice.

(M) Lack of co-expression of *Slc5a4a* (FISH, in green) and Ki67 (immunofluorescence, in magenta) in ileum cross sections of V, P7, and L7 mice. Scale bars, 100 μm.

(N) Co-expression analysis of *Slc5a4a* and *Fgfbp1* in gut rolls. FISH images showing cell classifications (*Slc5a4a*+ cell, green; *Fgfbp1*+ cell, magenta; double-positive in yellow; double-negative in gray) in ileal gut rolls of V (n = 4), P7 (n = 4), and L7 (n = 4) mice (left). Stacked bar plots showing cell proportions in each condition (center). The proportion of both *Slc5a4a*+ cell and *Slc5a4a*+ *Fgfbp1*+ double-positive cell is significantly increased during reproduction (right). Scale bars, 100 μm.

CBC, crypt base columnar; EC, enterocyte; P, progenitor; A, anterior.

p values are estimated using a two-way ANOVA in (C); a one-way ANOVA with Tukey's multiple comparisons test in (D); a linear mixed-effects model (lme4 and lmerTest R package; see STAR Methods for details) with a two-sample test in (K) and (L); and the propeller method (speckle R package; see STAR Methods for details) in (J) and (N). In all quantifications, $^{*}p < 0.05$, $^{**}p < 0.01$, $^{***}p < 0.001$.

See also Figures S3 and S4 and Tables S5 and S6.

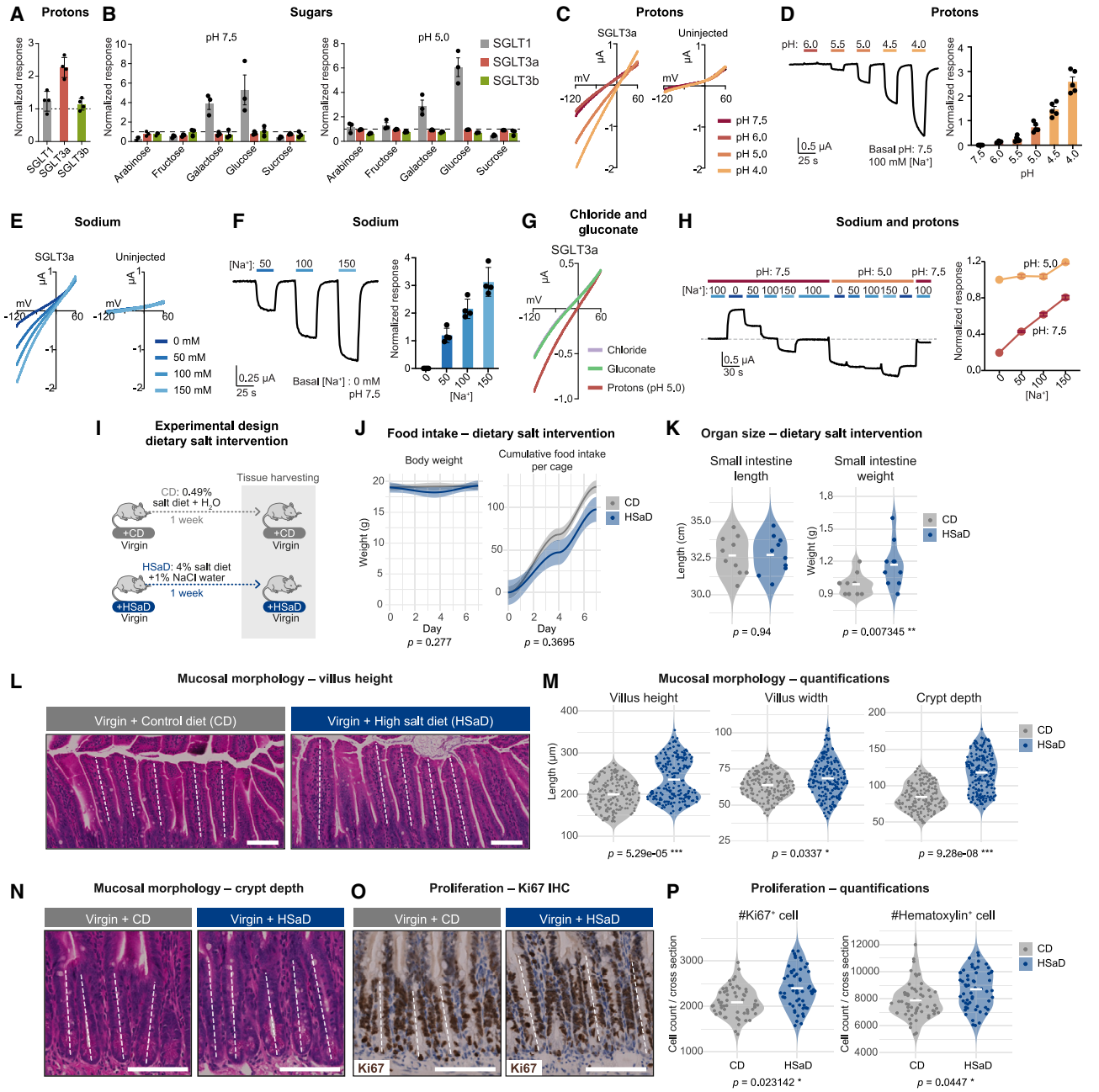

Figure 6. SGLT3a is a non-canonical pH- and sodium-sensitive transporter

(A) SGLT3a is pH-sensitive; peak inward currents are normalized to pH 7.5 ($n = 4$). Dashed line represents 1:1 response.

(B) SGLT3a and SGLT3b are insensitive to sugars irrespective of pH, while SGLT1 is sensitive to sugars ($n = 3$); peak inward currents are normalized relative to pH ($n = 3$). Dashed line represents 1:1 response.

(C and D) SGLT3a is activated by protons. Responses normalized to pH 7.5 were significantly larger at pH 4.5 and pH 4 ($p < 0.01$ and $p < 0.001$, respectively, $n = 5$).

(E and F) SGLT3a activity is enhanced by increasing sodium. Sodium-dependent responses normalized to 0 mM were significantly larger in the presence of 50, 100, or 150 mM sodium ($p < 0.01$, $n = 5$).

(G) SGLT3a inward transporter currents were not increased with chloride or gluconate.

(H) Inward transporter currents are increased with higher concentrations of Na^+ ions but only at neutral pH ($n = 4$). At pH 7.5, sodium-evoked currents were concentration-dependent ($p < 0.001$), but sodium did not enhance responses to pH 5.0 ($p < 0.001$, $n = 4$).

(I) Summary of experimental design.

(J) Body weight (left) and cumulative food intake (right) in control diet (CD)-fed and high-salt diet (HSaD)-fed mice ($n = 10$ per group).

(K) Small intestine length (left) and small intestine weight (right) in CD-fed and HSaD-fed mice ($n = 10$ per group).

(L) Representative H&E images of ileal villus height of CD-fed and HSaD-fed mice. Scale bars, 100 μm.

(legend continued on next page)

gluconeogenesis (*Pck1* and *Fbp1*), and fructose uptake, synthesis, and fructolysis (*GLUT5*, *Sord*, *Khk, Aldob*, and *Tkfc*) (Figure S4F; Table S6). Several genes involved in carbohydrate utilization (*Lct*, *Sis*, *Glut2*, *Khk*, *Aldob*, and *Tkfc*) were also upregulated in the isthmus progenitors of SGLT3a^{KO} females (Table S6).

Together, these experiments argue against roles for SGLT3a in supporting digestive physiology and whole-body energy balance but point to its substantial contribution to the reproductive remodeling of metabolism within SGLT3a-expressing enterocytes and adjacent isthmus progenitors.

SGLT3a is a non-canonical pH- and sodium-sensitive transporter

How might SGLT3a impact these processes? Previous work had pointed to non-canonical SGLT3a transport properties.[52] Consistently, and in contrast to the strong sensitivity of SGLT1 to glucose or galactose,[53–55] SGLT3a failed to respond to these sugars in electrophysiological recordings in *Xenopus laevis* oocytes (Figure 6B; see STAR Methods for details). Additional tests, including alternative sugars (sucrose, arabinose, and fructose) at acidic or neutral pH, still failed to elicit SGLT3a responses (Figure 6B). Instead, and also consistent with,[52] SGLT3a (but not SGLT1 or SGLT3b), responded to increasing proton concentrations (Figures 6A, 6C, and 6D). More unexpectedly, we observed that SGLT3a-expressing cells also responded to sodium (Figures 6E and 6F) and that pH-induced currents increased with higher concentrations of sodium ions (Figure 6H). These sodium responses appeared specific (no such modulation was observed in the presence of chloride; Figure 6G) and were only apparent at neutral pH, when the transporter may not be maximally active (Figure 6H).

Ions such as protons or sodium are commonly considered in the context of cellular processes such as transport or cell volume, but there is increasing realization that they play instructive roles during development.[56,57] To investigate possible roles in the context of intestinal remodeling, we supplemented the diet of virgin female mice with acid[58] or sodium[59] (see STAR Methods for details). While we failed to detect any proton-elicited effects (data not shown), sodium supplementation led to crypt-villus axis changes akin to reproductive changes: it resulted in longer and wider villi and deeper crypts and promoted progenitor proliferation in crypts (without increasing food intake, affecting body weight, or the length of the small intestine) (Figures 6I–6P; only a slight increase in the weight of the small intestine was apparent).

Thus, SGLT3a is neither activated nor modulated by sugars, but its transporter activity is sensitive to protons and sodium. Akin to reproduction, dietary sodium (but not acid) supplementation promotes epithelial proliferation and induces villus growth in virgin female mice.

Enterocyte SGLT3a sustains the reproductive expansion of Fgfbp1 progenitors and promotes villus growth

The above-described transcriptional effects and transport properties of SGLT3a prompted us to examine reproductive organ resizing in SGLT3^{KO} mutant females. Histologically, their intestinal mucosa is indistinguishable from that of controls prior to pregnancy (Figures 7A and 7B). However, despite no impairments in the remodeling of their crypts, the reproductive lengthening of villi was blunted in SGLT3^{KO} females (Figures 7C and 7D). Mutant females lacking SGLT3a alone displayed comparable phenotypes (Figures S5A and S5B). On average, SGLT3 is necessary for 45% of the villus growth increase triggered by reproduction (Figure 7E) without affecting organ sizes, including small intestinal length (Figures S5C and S5D).

To establish whether the villus growth-promoting effects of SGLT3 are specific to reproduction, we focused on dietary sugar excess, known to increase villus height.[60,61] Consistent with previous work,[61] control virgin female mice fed a normal diet plus *ad libitum* 25% high-fructose corn syrup (HFCS; see STAR Methods for details) have increased body mass and adiposity, increased liver weight, and longer small intestinal villi than mice on a normal diet and *ad libitum* water (Figures S6A–S6E). However, and unlike reproduction, HFCS feeding failed to upregulate SGLT3 expression in the small intestine (Figure S6F), and this is consistent with our electrophysiology data showing SGLT3a does not respond to sugars. By contrast, several genes coding for proteins involved in sugar transport/transformation were all significantly upregulated in the ileum in response to HFCS feeding (e.g., fructose transporter [GLUT5], GLUT2, and sucrose-isomaltase [Sis]; Figure S6F). Furthermore, the intestinal villi of SGLT3^{KO} virgin female mice elongated normally in response to HFCS, and we failed to observe any significant differences in body mass, liver weight, or intestinal length (Figures S6B–S6E). Hence, although diet and reproduction appear to make the gut grow in a similar way, the underlying mechanisms are distinct: SGLT3 sustains reproduction-specific villus growth.

How does reproductive SGLT3a induction in enterocytes lead to epithelial expansion? Having ruled out effects on food intake, digestive capacity, or ileal function (Figures S3D, S3G, and S3H), we assessed epithelial cell dynamics. In light of the reproductive increase in enterocyte size (Figures 2F and 2G), we considered possible SGLT3a effects on cell volume. However, the average villus cell area in lactating SGLT3^{KO} mice was comparable to that of lactating control littermates (Figure 7F). Similarly, we observed comparable levels and patterns of apoptosis in the mutant mice (Table S1). By contrast, EdU incorporation and Ki67 staining indicated that progenitor proliferation and migration of the differentiated progeny were both decreased in lactating SGLT3^{KO} female mice (Figures 7G–7I, confirmed in

(M) Morphometric quantifications of ileal villus height, villus width, and crypt depth in CD-fed and HSaD-fed mice (n = 10 per group).
(N and O) Representative H&E images of ileal crypt depth (N) and anti-Ki67 immunohistochemistry (IHC) staining in ileal crypt (O) of CD-fed and HSaD-fed mice. Scale bars, 100 μm.
(P) Quantifications of the number of Ki67+ cells per ileal cross sections in CD-fed and HSaD-fed mice (n = 10 per group).
p values are estimated using a one-way ANOVA with Kruskal-Wallis multiple comparisons test in (D) and (F); a two-way ANOVA with Dunnett's multiple comparisons test in (H); and a linear mixed-effects model (lme4 and lmerTest R package; see STAR Methods for details) with a two-sample test in (J), (K), (M), and (P). In all quantifications, $^{*}p < 0.05$, $^{**}p < 0.01$, $^{***}p < 0.001$.

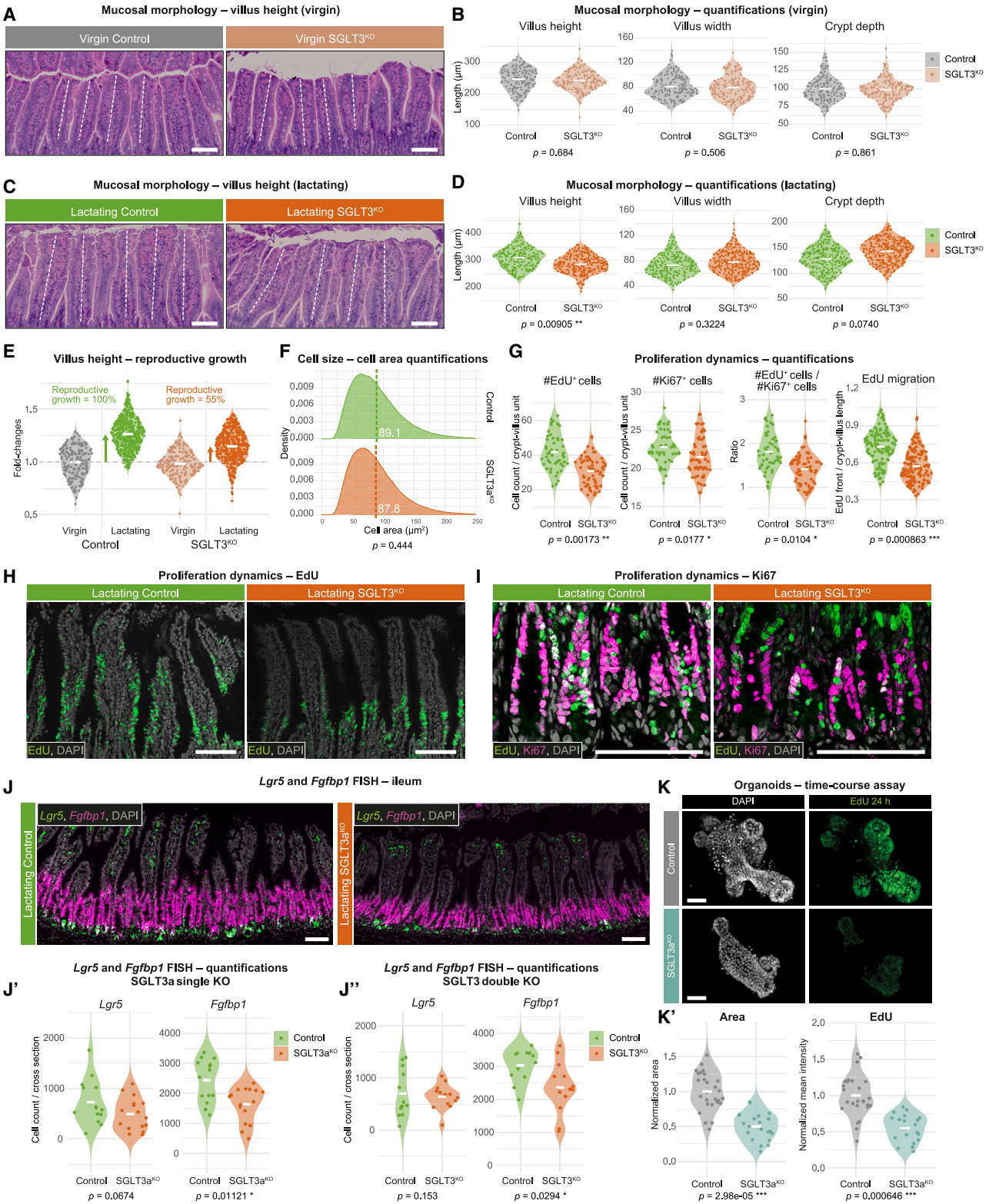

Figure 7. Enterocyte SGLT3a sustains the reproductive expansion of Fgfbp1 progenitors and promotes villus growth

(A and C) Representative H&E images of ileum of V (A) and L (C) control and SGLT3^{KO} female mice. Scale bars, 100 µm.

(B and D) Morphometric quantifications of ileal villus height of V (B) and L (D) control and SGLT3^{KO} female mice (n = 8–9 per group).

(legend continued on next page)

mice lacking SGLT3a only; Figures S5E–S5G). The *Lgr5*-positive CBC population was unaffected by the SGLT3 mutation (Figures 7J–7J″). By contrast, there was a substantial reduction in the number of Fgfbp1-positive progenitors (Figures 7J–7J″; but not in Fgfbp1 expression levels within them; data not shown). Reduced proliferation (as assessed by organoid area and EdU incorporation) was also apparent *ex vivo* in organoids derived from SGLT3a mutant mice, confirming the intestinal origin of the SGLT3a mutant phenotypes (Figures 7K, 7K′, S5H, and S5I).

These findings indicate that SGLT3a is specifically required for the reproductive expansion of the small intestinal epithelium. SGLT3a in enterocytes extrinsically supports the reproductive expansion of the adjacent Fgfbp1-positive isthmus progenitors.

DISCUSSION

We have described the reproductive growth of the intestine at the tissue, cellular, and molecular levels. Reproductive remodeling is distinct from other types of adult intestinal growth (e.g., dietary or microbial) and involves two processes that can be genetically uncoupled: elongation of the small intestine and expansion of its epithelium. Both these aspects of remodeling occur during pregnancy and persist in lactation but differ in their reversibility and underlying genetic mechanisms. While the reproductive expansion of the intestinal epithelium is sustained by SGLT3a and is fully and rapidly reversible, intestinal elongation is SGLT3a-independent and partially irreversible. From the perspective of epithelial remodeling, it will be interesting to explore how reproductive and regenerative epithelial plasticity differ and whether the intestine responds differently to damage during pregnancy.

What upregulates SGLT3a expression and initiates epithelial remodeling? Our initial data are consistent with hormonal input. Indeed, in pseudopregnant females (in which mating to sterile males leads to a hormonal surge routinely leveraged in *in vitro* fertilization experiments), we observe some villus growth and intestinal elongation 7 days after mating despite not having an actual pregnancy (Figures S7A–S7D). In our single-cell transcriptome data, and consistent with,[62] the prolactin receptor is broadly expressed in epithelial cells (Figure S7E), and prolactin treatment of organoids leads to robust and specific induction of *Slc5a4a* (no *Slc5a4b* upregulation was observed; Figure S7F). Contributions from other intestinal cell populations are also likely.[63] From this perspective, it will be of interest to investigate whether mesenchymal RANKL (encoded by *Tnfsf11*), recently shown to support epithelial expansion,[15] is required for the reproductive upregulation of SGLT3a expression. Finally, the reproductive changes in EE hormone gene expression we have observed (Figures S2D and S2D′) are also intriguing in this regard. Possible systemic effects of these changes and/or contributions of these hormones to intestinal remodeling deserve further investigation.

SGLT3a modulates two under-investigated processes: the expansion of the Fgfbp1-positive isthmus progenitors and the migration of differentiating cells up the villus. The latter was only recently recognized as an active, actin-mediated process.[64] Reproduction triggered, SGLT3a-modulated ionic currents in the SGLT3a bottom/mid-villus enterocytes may interact with the cytoskeleton to sustain active migration. But how might SGLT3a from enterocytes extrinsically sustain the expansion of Fgfbp1 isthmus progenitors? In light of the physical proximity between SGLT3a enterocytes and the Fgfbp1-expressing isthmus progenitors, we suggest that the enhanced proliferation of these (but not the Lgr5-positive) progenitors during reproduction may require metabolic coupling between them and SGLT3a-expressing enterocytes, akin to that described for Paneth cells and Lgr5-positive CBCs.[65] The sodium transport properties of SGLT3a may be important in this regard, given that dietary sodium supplementation recapitulates the effects of SGLT3a on villus growth and progenitor proliferation in virgin female mice (Figures 6I–6P). The finding that sodium can make villi grow is of potential significance given its increasing prevalence in our diets: only macronutrients such as lipids or sugars had been considered in this regard.

Does SGLT3a-sustained villus growth matter? SGLT3a mutation does not lead to changes in overall digestive capacity but does result in dampened progenitor proliferation and villus growth. Enterocytes are known to differ in their absorptive properties and metabolism depending on their position on the villus.[6,49,66,67] SGLT3a might alter the nature of what the intestine absorbs (rather than its overall digestive capacity) in two ways: by sustaining the metabolic remodeling of SGLT3a-positive enterocytes cell intrinsically and by altering the enterocyte composition of villi as a result of its effects on progenitor proliferation and/or migration. SGLT3a-mediated epithelial remodeling may help sustain reproductive output. Consistent with this

(E) Morphometric quantifications of ileal villus height: reproduction-induced elongation is blunted by 55% in SGLT3^{KO} mice (n = 8–9 per group). Lactating mice post-1st and 2nd pregnancy were pooled as "lactating" conditions as their villus height was comparable (Figure 1F).
(F) Villus cell size quantifications in ileums of lactating control (n = 15) and lactating SGLT3a^{KO} (n = 13) mice. See STAR Methods for details.
(G) Quantifications of proliferation markers in the ileum of lactating control (n = 9) and SGLT3^{KO} (n = 12) mice.
(H and I) Representative EdU (H) and anti-Ki67 (I) staining of ileums of lactating control and SGLT3^{KO} mice. Gut tissues were harvested 24 h after injection EdU injection. Scale bars, 100 μm.
(J) Representative FISH images (*Lgr5*, green; *Fgfbp1*, magenta) of ileal cross sections of lactating control and SGLT3a^{KO}. Scale bars, 100 μm.
(J′ and J″) Number of *Lgr5*+ or *Fgfbp1*+ cells per cross section (lactating control, n = 8; lactating SGLT3a^{KO}, n = 9 in J′, and lactating control, n = 8; lactating SGLT3^{KO}, n = 9 in J″).
(K and K′) Intestinal organoids derived from lactating control (n = 5) or SGLT3a^{KO} (n = 3) mice (K) and quantifications of normalized organoid area and EdU signal intensity (K′). Scale bars, 50 μm.
Original sections analyzed in (B) and (E) are also shown in Figures 1F and S1H (control).
p values are estimated using a linear mixed-effects model (lme4 and lmerTest R package; see STAR Methods for details) with a two-sample test in (B), (D), (F), (G), (J′), (J″), and (K′). In all quantifications, *p < 0.05, **p < 0.01, ***p < 0.001.
See also Figures S5–S7 and Table S6.

idea, the viability of pups born to SGLT3a mutant mothers is reduced by lactation day 7 (Figure S5J), and milk composition is different in mice in which intestinal remodeling is independently impaired.[15]

More generally, reduced transit and the epithelial expansion of the intestine are both regarded as reproductive adaptations that maximize digestive capacity as nutritional demands increase. From this perspective, we were intrigued by our finding that digestive efficiency is reduced (rather than increased or maintained) in wild-type lactating mice (Figure S3H′). Reduced transit might instead be maladaptive, and the epithelium may expand to (insufficiently) compensate for this. It is also possible that the dramatic increase in ingested food, particularly in lactation, renders a certain amount of intestinal content unavailable for absorption, despite the increased absorptive area resulting from epithelial expansion. The reversibility of these processes also deserves further investigation, and it may have made evolutionary sense to maintain a larger gut after a first pregnancy to sustain multiple pregnancies in nutrient-scarce conditions, but this larger gut could contribute to weight retention and obesity in our world of nutrient excess and reduced reproductive output.[30,68] These considerations provide an impetus for understanding organ- and state-specific growth programs, which could in the future be leveraged to prevent maladaptive consequences of such growth and/or improve pregnancy care.

Limitations of the study

Although we validated contributions of SGLT3a to the reproductive expansion of the intestinal epithelium in both single SGLT3a and double SGLT3a/b knockout as well as intestinal organoids derived from these knockout mice, we cannot currently exclude that the reduced pup viability we have observed in these mice is caused by the absence of SGLT3a in other organs. We also note that both our analysis of reproductive remodeling of the intestine and that of Onji et al.[15] have so far focused on the expansion of its epithelium. It will be of interest to explore the ability of non-epithelial layers to contribute to the reproductive growth of the intestine—particularly to gut tube elongation, whose partial irreversibility could lead to long-lasting post-pregnancy effects.

RESOURCE AVAILABILITY

Lead contact

Further information and requests for resources and reagents should be directed to and will be fulfilled by the lead contact, Irene Miguel-Aliaga (irene.miguelaliaga@crick.ac.uk).

Materials availability

Materials used in this study are listed in the key resources table. All unique/stable reagents generated in this study are available from the lead contact with a completed Materials Transfer Agreement.

Data and code availability

- All data reported in this paper will be shared by the lead contact upon request. Transcriptome and spatial data have been deposited at NCBI GEO under accession GEO: GSE247929 (GEO: GSE247923, GSE 247925, GSE247926, and GSE247927) and GEO: GSE285027, respectively, and additional data have been deposited in Mendeley Data: https://doi.org/10.17632/f239gwztnm.1 and are publicly available as of the date of publication. Scripts for analysis of Xenium data are available on GitHub at https://github.com/AnnaLaddach/MaternalIntestineXenium.
- This paper does not report original code.
- Any additional information required to reanalyze the data reported in this paper is available from the lead contact upon request.

ACKNOWLEDGMENTS

We thank staff at the Imperial College Central Biological Services for support with mouse breeding and maintenance. We are grateful to Chad Whilding for imaging quantification advice, Boris Lenhard for statistical advice, Lorraine Lawrence for histology support, Véronique Kalck for support with the organoid isolation, Ayaka Ameku for illustrations, and Bryon Silva for comments. This work was funded by an ERC Advanced Grant (ERCAdG 787470 "IntraGutSex"), a UKRI Horizon Europe guarantee grant (EPSRC-ERC EP/Y03298/1) to I.M.-A., and an NIH grant (R35GM142697) to N.W.B. I.M.-A. was also funded by MRC intramural funding and the Francis Crick Institute, which receives its core funding from Cancer Research UK (FC001317 and FC001175), the UK Medical Research Council (FC001317 and FC001175), and the Wellcome Trust (FC001317 and FC001175). T.A. was a recipient of Fellowships from the Japan Society for the Promotion of Science and the Uehara Memorial Foundation. H.B. held a Chain-Florey Clinical Research Fellowship supported by the National Institute for Health Research (NIHR) Imperial Biomedical Research Centre (BRC) and the MRC Laboratory of Medical Sciences (LMS). D.J.W. was funded by MRC grant MC-A654-5QB40, and M.S. acknowledges the support from the Czech Science Foundation (grant 21-19640M).

AUTHOR CONTRIBUTIONS

Conceptualization, T.A. and I.M.-A.; investigation, T.A. (most experiments); A.L. and V.P. (computational analysis for Xenium spatial assay); H.B. (RT-qPCR of different small intestine regions); A.M., E.E.I., and D.J.W. (BioDAQ); L.S.R., P.M.V., and N.W.B. (electrophysiology); C. Schwayer and P.L. (organoid time course assay); E.N. (histology support); I.R.T. and H.M.C. (Ussing chamber assay); J.-L.T. and F.L. (probiotics experiments); U.K.G. and M.S. (germ-free experiments); Y.-F.W., S.J., and G.Y. (computational analysis for bulk and single-cell RNA-seq); A.C.-M. (IF staining for validating RNA-seq data); C.A. (bulk RNA-seq of different small intestine regions); S.G. and M.R.-C. (organoids metabolic assay); A.M., B.O., L.M., and K.G.M. (*in vivo* prolactin administration); I.A., K.L.C., and L.G. (running transcriptome and Xenium spatial assay); B.P. (FACS sorting support); and A.J.F. and C. Studd (mouse genotyping and breeding support); visualization, T.A.and I.M.-A.; writing – original draft, T.A., H.B., and I.M.-A.; writing – review & editing, T.A. and I.M.-A., with input from all the authors; supervision, I.M.-A.

DECLARATION OF INTERESTS

The authors declare no competing interests.

STAR★METHODS

Detailed methods are provided in the online version of this paper and include the following:

- KEY RESOURCES TABLE
- EXPERIMENTAL MODEL AND STUDY PARTICIPANT DETAILS
  - Mice
  - Germ-free mice
  - Probiotics supplementation
  - Mouse intestinal organoids
- METHOD DETAILS
  - Metabolic measurements
  - Bomb calorimetry
  - Immunohistochemistry (IHC)
  - Immunofluorescence (IF)
  - Single molecule fluorescence in situ hybridization (smFISH)
  - RNA extraction and quantitative RT-PCR

SUPPLEMENTAL INFORMATION

Supplemental information can be found online at https://doi.org/10.1016/j.cell.2025.02.015.

Received: December 19, 2023
Revised: December 12, 2024
Accepted: February 19, 2025
Published: March 19, 2025
Corrected online: April 23, 2025

REFERENCES

1. Cheng, H., and Leblond, C.P. (1974). Origin, differentiation and renewal of the four main epithelial cell types in the mouse small intestine. I. Columnar cell. Am. J. Anat. *141*, 461–479. https://doi.org/10.1002/aja.1001410403.
2. Cheng, H., and Leblond, C.P. (1974). Origin, differentiation and renewal of the four main epithelial cell types in the mouse small intestine. V. Unitarian Theory of the origin of the four epithelial cell types. Am. J. Anat. *141*, 537–561. https://doi.org/10.1002/aja.1001410407.
3. Clevers, H. (2013). The intestinal crypt, a prototype stem cell compartment. Cell *154*, 274–284. https://doi.org/10.1016/j.cell.2013.07.004.
4. Gehart, H., and Clevers, H. (2019). Tales from the crypt: new insights into intestinal stem cells. Nat. Rev. Gastroenterol. Hepatol. *16*, 19–34. https://doi.org/10.1038/s41575-018-0081-y.
5. van der Flier, L.G., and Clevers, H. (2009). Stem cells, self-renewal, and differentiation in the intestinal epithelium. Annu. Rev. Physiol. *71*, 241–260. https://doi.org/10.1146/annurev.physiol.010908.163145.
6. Beumer, J., and Clevers, H. (2021). Cell fate specification and differentiation in the adult mammalian intestine. Nat. Rev. Mol. Cell Biol. *22*, 39–53. https://doi.org/10.1038/s41580-020-0278-0.
7. Capdevila, C., Miller, J., Cheng, L., Kornberg, A., George, J.J., Lee, H., Botella, T., Moon, C.S., Murray, J.W., Lam, S., et al. (2024). Time-resolved fate mapping identifies the intestinal upper crypt zone as an origin of Lgr5+ crypt base columnar cells. Cell *187*, 3039–3055.e14. https://doi.org/10.1016/j.cell.2024.05.001.
8. Malagola, E., Vasciaveo, A., Ochiai, Y., Kim, W., Zheng, B., Zanella, L., Wang, A.L.E., Middelhoff, M., Nienhüser, H., Deng, L., et al. (2024). Isthmus progenitor cells contribute to homeostatic cellular turnover and support regeneration following intestinal injury. Cell *187*, 3056–3071.e17. https://doi.org/10.1016/j.cell.2024.05.004.
9. Stojanović, O., Miguel-Aliaga, I., and Trajkovski, M. (2022). Intestinal plasticity and metabolism as regulators of organismal energy homeostasis. Nat. Metab. *4*, 1444–1458. https://doi.org/10.1038/s42255-022-00679-6.
10. Poo, L.J., Lew, W., and Addis, T. (1939). Protein anabolism of organs and tissues during pregnancy and lactation. J. Biol. Chem. *128*, 69–77. https://doi.org/10.1016/S0021-9258(18)73730-7.
11. Fell, B.F., Smith, K.A., and Campbell, R.M. (1963). Hypertrophic and hyperplastic changes in the alimentary canal of the lactating rat. J. Pathol. Bacteriol. *85*, 179–188. https://doi.org/10.1002/path.1700850117.
12. Hammond, K.A. (1997). Adaptation of the maternal intestine during lactation. J. Mammary Gland Biol. Neoplasia *2*, 243–252. https://doi.org/10.1023/a:1026332304435.
13. Souders, H.J., and Morgan, A.F. (1957). Weight and composition of organs during the reproductive cycle in the rat. Am. J. Physiol. *191*, 1–7. https://doi.org/10.1152/ajplegacy.1957.191.1.1.
14. Speakman, J.R. (2008). The physiological costs of reproduction in small mammals. Philos. Trans. R. Soc. Lond. B Biol. Sci. *363*, 375–398. https://doi.org/10.1098/rstb.2007.2145.
15. Onji, M., Sigl, V., Lendl, T., Novatchkova, M., Ullate-Agote, A., Andersson-Rolf, A., Kozieradzki, I., Koglgruber, R., Pai, T.P., Lichtscheidl, D., et al. (2025). RANK drives structured intestinal epithelial expansion during pregnancy. Nature *637*, 156–166. https://doi.org/10.1038/s41586-024-08284-1.
16. Beyaz, S., Mana, M.D., Roper, J., Kedrin, D., Saadatpour, A., Hong, S.J., Bauer-Rowe, K.E., Xifaras, M.E., Akkad, A., Arias, E., et al. (2016). High-fat diet enhances stemness and tumorigenicity of intestinal progenitors. Nature *531*, 53–58. https://doi.org/10.1038/nature17173.
17. Chevalier, C., Stojanović, O., Colin, D.J., Suarez-Zamorano, N., Tarallo, V., Veyrat-Durebex, C., Rigo, D., Fabbiano, S., Stevanović, A., Hagemann, S., et al. (2015). Gut Microbiota Orchestrates Energy Homeostasis during Cold. Cell *163*, 1360–1374. https://doi.org/10.1016/j.cell.2015.11.004.
18. McCullogh, J.S., Ratcliffe, B., Mandir, N., Carr, K.E., and Goodlad, R.A. (1998). Dietary fibre and intestinal microflora: effects on intestinal morphometry and crypt branching. Gut *42*, 799–806. https://doi.org/10.1136/gut.42.6.799.
19. Yilmaz, Ö.H., Katajisto, P., Lamming, D.W., Gültekin, Y., Bauer-Rowe, K.E., SenGupta, S., Birsoy, K., Dursun, A., Yilmaz, V.O., Selig, M., et al. (2012). mTORC1 in the Paneth cell niche couples intestinal stem-cell function to calorie intake. Nature *486*, 490–495. https://doi.org/10.1038/nature11163.
20. Hadjieconomou, D., King, G., Gaspar, P., Mineo, A., Blackie, L., Ameku, T., Studd, C., de Mendoza, A., Diao, F., White, B.H., et al. (2020). Enteric neurons increase maternal food intake during reproduction. Nature *587*, 455–459. https://doi.org/10.1038/s41586-020-2866-8.
21. Hudry, B., Khadayate, S., and Miguel-Aliaga, I. (2016). The sexual identity of adult intestinal stem cells controls organ size and plasticity. Nature *530*, 344–348. https://doi.org/10.1038/nature16953.
22. Reiff, T., Jacobson, J., Cognigni, P., Antonello, Z., Ballesta, E., Tan, K.J., Yew, J.Y., Dominguez, M., and Miguel-Aliaga, I. (2015). Endocrine remodelling of the adult intestine sustains reproduction in Drosophila. eLife *4*, e06930. https://doi.org/10.7554/eLife.06930.
23. Ahmed, S.M.H., Maldera, J.A., Krunic, D., Paiva-Silva, G.O., Pénalva, C., Teleman, A.A., and Edgar, B.A. (2020). Fitness trade-offs incurred by ovary-to-gut steroid signalling in Drosophila. Nature *584*, 415–419. https://doi.org/10.1038/s41586-020-2462-y.
24. Ameku, T., Yoshinari, Y., Texada, M.J., Kondo, S., Amezawa, K., Yoshizaki, G., Shimada-Niwa, Y., and Niwa, R. (2018). Midgut-derived neuropeptide F controls germline stem cell proliferation in a mating-dependent manner. PLoS Biol. *16*, e2005004. https://doi.org/10.1371/journal.pbio.2005004.
25. Kandelouei, T., Houghton, M.E., Lewis, M.R., Keller, C.C., Marchetti, M., Kang, X., and Edgar, B.A. (2024). Mating and ecdysone signaling modify growth, metabolism, and digestive efficiency in the female Drosophila gut. Preprint at bioRxiv. https://doi.org/10.1101/2024.11.19.624434.
26. White, M.A., Bonfini, A., Wolfner, M.F., and Buchon, N. (2021). Drosophila melanogaster sex peptide regulates mated female midgut morphology and physiology. Proc. Natl. Acad. Sci. USA *118*, e2018112118. https://doi.org/10.1073/pnas.2018112118.
27. Zipper, L., Jassmann, D., Burgmer, S., Görlich, B., and Reiff, T. (2020). Ecdysone steroid hormone remote controls intestinal stem cell fate decisions via the PPARgamma-homolog Eip75B in Drosophila. eLife *9*, e55795. https://doi.org/10.7554/eLife.55795.

28. Zipper, L., Corominas-Murtra, B., and Reiff, T. (2025). Steroid hormone-induced wingless ligands tune female intestinal size in Drosophila. Nat. Commun. *16*, 436. https://doi.org/10.1038/s41467-024-55664-2.

29. Campbell, R.M., and Fell, B.F. (1964). Gastro-Intestinal Hypertrophy in the Lactating Rat and Its Relation to Food Intake. J. Physiol. *171*, 90–97. https://doi.org/10.1113/jphysiol.1964.sp007363.

30. Casirola, D.M., and Ferraris, R.P. (2003). Role of the small intestine in postpartum weight retention in mice. Am. J. Clin. Nutr. *78*, 1178–1187. https://doi.org/10.1093/ajcn/78.6.1178.

31. Salic, A., and Mitchison, T.J. (2008). A chemical method for fast and sensitive detection of DNA synthesis in vivo. Proc. Natl. Acad. Sci. USA *105*, 2415–2420. https://doi.org/10.1073/pnas.0712168105.

32. Gerdes, J., Schwab, U., Lemke, H., and Stein, H. (1983). Production of a mouse monoclonal antibody reactive with a human nuclear antigen associated with cell proliferation. Int. J. Cancer *31*, 13–20. https://doi.org/10.1002/ijc.2910310104.

33. Potten, C.S. (1998). Stem cells in gastrointestinal epithelium: numbers, characteristics and death. Philos. Trans. R. Soc. Lond. B Biol. Sci. *353*, 821–830. https://doi.org/10.1098/rstb.1998.0246.

34. Chaker, Z., Segalada, C., Kretz, J.A., Acar, I.E., Delgado, A.C., Crotet, V., Moor, A.E., and Doetsch, F. (2023). Pregnancy-responsive pools of adult neural stem cells for transient neurogenesis in mothers. Science *382*, 958–963. https://doi.org/10.1126/science.abo5199.

35. Fernandes-Alnemri, T., Litwack, G., and Alnemri, E.S. (1994). CPP32, a novel human apoptotic protein with homology to Caenorhabditis elegans cell death protein Ced-3 and mammalian interleukin-1 beta-converting enzyme. J. Biol. Chem. *269*, 30761–30764. https://doi.org/10.1016/S0021-9258(18)47344-9.

36. Gorczyca, W., Bruno, S., Darzynkiewicz, R., Gong, J., and Darzynkiewicz, Z. (1992). DNA strand breaks occurring during apoptosis - their early insitu detection by the terminal deoxynucleotidyl transferase and nick translation assays and prevention by serine protease inhibitors. Int. J. Oncol. *1*, 639–648. https://doi.org/10.3892/ijo.1.6.639.

37. Nicholson, D.W., Ali, A., Thornberry, N.A., Vaillancourt, J.P., Ding, C.K., Gallant, M., Gareau, Y., Griffin, P.R., Labelle, M., and Lazebnik, Y.A. (1995). Identification and inhibition of the ICE/CED-3 protease necessary for mammalian apoptosis. Nature *376*, 37–43. https://doi.org/10.1038/376037a0.

38. Hall, P.A., Coates, P.J., Ansari, B., and Hopwood, D. (1994). Regulation of cell number in the mammalian gastrointestinal tract: the importance of apoptosis. J. Cell Sci. *107*, 3569–3577. https://doi.org/10.1242/jcs.107.12.3569.

39. Stojanović, O., Altirriba, J., Rigo, D., Spiljar, M., Evrard, E., Roska, B., Fabbiano, S., Zamboni, N., Maechler, P., Rohner-Jeanrenaud, F., et al. (2021). Dietary excess regulates absorption and surface of gut epithelium through intestinal PPARα. Nat. Commun. *12*, 7031. https://doi.org/10.1038/s41467-021-27133-7.

40. Datta, U.K., Datta, A.N., and Mukherjee, S. (1995). Role of hyperphagia in structural changes of small intestine during lactation. Indian J. Physiol. Pharmacol. *39*, 259–262.

41. Clarke, G.S., Gatford, K.L., Young, R.L., Grattan, D.R., Ladyman, S.R., and Page, A.J. (2021). Maternal adaptations to food intake across pregnancy: Central and peripheral mechanisms. Obesity (Silver Spring) *29*, 1813–1824. https://doi.org/10.1002/oby.23224.

42. Ladyman, S.R., Fieldwick, D.M., and Grattan, D.R. (2012). Suppression of leptin-induced hypothalamic JAK/STAT signalling and feeding response during pregnancy in the mouse. Reproduction *144*, 83–90. https://doi.org/10.1530/REP-12-0112.

43. Koren, O., Goodrich, J.K., Cullender, T.C., Spor, A., Laitinen, K., Backhed, H.K., Gonzalez, A., Werner, J.J., Angenent, L.T., Knight, R., et al. (2012). Host remodeling of the gut microbiome and metabolic changes during pregnancy. Cell *150*, 470–480. https://doi.org/10.1016/j.cell.2012.07.008.

44. Al-Asmakh, M., and Zadjali, F. (2015). Use of Germ-Free Animal Models in Microbiota-Related Research. J. Microbiol. Biotechnol. *25*, 1583–1588. https://doi.org/10.4014/jmb.1501.01039.

45. Schwarzer, M., Gautam, U.K., Makki, K., Lambert, A., Brabec, T., Joly, A., Šrůtková, D., Poinsot, P., Novotná, T., Geoffroy, S., et al. (2023). Microbe-mediated intestinal NOD2 stimulation improves linear growth of undernourished infant mice. Science *379*, 826–833. https://doi.org/10.1126/science.ade9767.

46. Schwarzer, M., Makki, K., Storelli, G., Machuca-Gayet, I., Srutkova, D., Hermanova, P., Martino, M.E., Balmand, S., Hudcovic, T., Heddi, A., et al. (2016). Lactobacillus plantarum strain maintains growth of infant mice during chronic undernutrition. Science *351*, 854–857. https://doi.org/10.1126/science.aad8588.

47. Storelli, G., Defaye, A., Erkosar, B., Hols, P., Royet, J., and Leulier, F. (2011). Lactobacillus plantarum promotes Drosophila systemic growth by modulating hormonal signals through TOR-dependent nutrient sensing. Cell Metab. *14*, 403–414. https://doi.org/10.1016/j.cmet.2011.07.012.

48. Haber, A.L., Biton, M., Rogel, N., Herbst, R.H., Shekhar, K., Smillie, C., Burgin, G., Delorey, T.M., Howitt, M.R., Katz, Y., et al. (2017). A single-cell survey of the small intestinal epithelium. Nature *551*, 333–339. https://doi.org/10.1038/nature24489.

49. Moor, A.E., Harnik, Y., Ben-Moshe, S., Massasa, E.E., Rozenberg, M., Eilam, R., Bahar Halpern, K., and Itzkovitz, S. (2018). Spatial Reconstruction of Single Enterocytes Uncovers Broad Zonation along the Intestinal Villus Axis. Cell *175*, 1156–1167.e15. https://doi.org/10.1016/j.cell.2018.08.063.

50. Soták, M., Casselbrant, A., Rath, E., Zietek, T., Strömstedt, M., Adingupu, D.D., Karlsson, D., Fritsch Fredin, M., Ergang, P., Pácha, J., et al. (2021). Intestinal sodium/glucose cotransporter 3 expression is epithelial and downregulated in obesity. Life Sci. *267*, 118974. https://doi.org/10.1016/j.lfs.2020.118974.

51. Gorboulev, V., Schürmann, A., Vallon, V., Kipp, H., Jaschke, A., Klessen, D., Friedrich, A., Scherneck, S., Rieg, T., Cunard, R., et al. (2012). Na(+)-D-glucose cotransporter SGLT1 is pivotal for intestinal glucose absorption and glucose-dependent incretin secretion. Diabetes *61*, 187–196. https://doi.org/10.2337/db11-1029.

52. Barcelona, S., Menegaz, D., and Díez-Sampedro, A. (2012). Mouse SGLT3a generates proton-activated currents but does not transport sugar. Am. J. Physiol. Cell Physiol. *302*, C1073–C1082. https://doi.org/10.1152/ajpcell.00436.2011.

53. Díez-Sampedro, A., Wright, E.M., and Hirayama, B.A. (2001). Residue 457 controls sugar binding and transport in the Na(+)/glucose cotransporter. J. Biol. Chem. *276*, 49188–49194. https://doi.org/10.1074/jbc.M108286200.

54. Parent, L., Supplisson, S., Loo, D.D., and Wright, E.M. (1992). Electrogenic properties of the cloned Na+/glucose cotransporter: I. Voltage-clamp studies. J. Membr. Biol. *125*, 49–62. https://doi.org/10.1007/BF00235797.

55. Parent, L., Supplisson, S., Loo, D.D., and Wright, E.M. (1992). Electrogenic properties of the cloned Na+/glucose cotransporter: II. A transport model under nonrapid equilibrium conditions. J. Membr. Biol. *125*, 63–79. https://doi.org/10.1007/BF00235798.

56. Oginuma, M., Harima, Y., Tarazona, O.A., Diaz-Cuadros, M., Michaut, A., Ishitani, T., Xiong, F., and Pourquié, O. (2020). Intracellular pH controls WNT downstream of glycolysis in amniote embryos. Nature *584*, 98–101. https://doi.org/10.1038/s41586-020-2428-0.

57. Yang, Q., Xue, S.L., Chan, C.J., Rempfler, M., Vischi, D., Maurer-Gutierrez, F., Hiiragi, T., Hannezo, E., and Liberali, P. (2021). Cell fate coordinates mechano-osmotic forces in intestinal crypt formation. Nat. Cell Biol. *23*, 733–744. https://doi.org/10.1038/s41556-021-00700-2.

58. Wolf, K.J., Daft, J.G., Tanner, S.M., Hartmann, R., Khafipour, E., and Lorenz, R.G. (2014). Consumption of acidic water alters the gut microbiome and decreases the risk of diabetes in NOD mice. J. Histochem. Cytochem. *62*, 237–250. https://doi.org/10.1369/0022155413519650.

59. Binger, K.J., Gebhardt, M., Heinig, M., Rintisch, C., Schroeder, A., Neuhofer, W., Hilgers, K., Manzel, A., Schwartz, C., Kleinewietfeld, M., et al.

(2015). High salt reduces the activation of IL-4- and IL-13-stimulated macrophages. J. Clin. Invest. *125*, 4223–4238. https://doi.org/10.1172/JCI80919.

60. Aliluev, A., Tritschler, S., Sterr, M., Oppenländer, L., Hinterdobler, J., Greisle, T., Irmler, M., Beckers, J., Sun, N., Walch, A., et al. (2021). Diet-induced alteration of intestinal stem cell function underlies obesity and prediabetes in mice. Nat. Metab. *3*, 1202–1216. https://doi.org/10.1038/s42255-021-00458-9.

61. Taylor, S.R., Ramsamooj, S., Liang, R.J., Katti, A., Pozovskiy, R., Vasan, N., Hwang, S.K., Nahiyaan, N., Francoeur, N.J., Schatoff, E.M., et al. (2021). Dietary fructose improves intestinal cell survival and nutrient absorption. Nature *597*, 263–267. https://doi.org/10.1038/s41586-021-03827-2.

62. Aoki, M., Wartenberg, P., Grünewald, R., Phillipps, H.R., Wyatt, A., Grattan, D.R., and Boehm, U. (2019). Widespread Cell-Specific Prolactin Receptor Expression in Multiple Murine Organs. Endocrinology *160*, 2587–2599. https://doi.org/10.1210/en.2019-00234.

63. Corral, D., Ansaldo, E., Delaleu, J., Pichler, A.C., Kabat, J., Oguz, C., Teijeiro, A., Yong, D., Abid, M., Rivera, C.A., et al. (2025). Mammary intraepithelial lymphocytes promote lactogenesis and offspring fitness. Cell *188*. https://doi.org/10.1016/j.cell.2025.01.028.

64. Krndija, D., El Marjou, F., Guirao, B., Richon, S., Leroy, O., Bellaiche, Y., Hannezo, E., and Matic Vignjevic, D. (2019). Active cell migration is critical for steady-state epithelial turnover in the gut. Science *365*, 705–710. https://doi.org/10.1126/science.aau3429.

65. Rodríguez-Colman, M.J., Schewe, M., Meerlo, M., Stigter, E., Gerrits, J., Pras-Raves, M., Sacchetti, A., Hornsveld, M., Oost, K.C., Snippert, H.J., et al. (2017). Interplay between metabolic identities in the intestinal crypt supports stem cell function. Nature *543*, 424–427. https://doi.org/10.1038/nature21673.

66. Zhang, J., Tian, R., Liu, J., Yuan, J., Zhang, S., Chi, Z., Yu, W., Yu, Q., Wang, Z., Chen, S., et al. (2024). A two-front nutrient supply environment fuels small intestinal physiology through differential regulation of nutrient absorption and host defense. Cell *187*, 6251–6271.e20. https://doi.org/10.1016/j.cell.2024.08.012.

67. Zwick, R.K., Kasparek, P., Palikuqi, B., Viragova, S., Weichselbaum, L., McGinnis, C.S., McKinley, K.L., Rathnayake, A., Vaka, D., Nguyen, V., et al. (2024). Epithelial zonation along the mouse and human small intestine defines five discrete metabolic domains. Nat. Cell Biol. *26*, 250–262. https://doi.org/10.1038/s41556-023-01337-z.

68. Gore, S.A., Brown, D.M., and West, D.S. (2003). The role of postpartum weight retention in obesity among women: a review of the evidence. Ann. Behav. Med. *26*, 149–159. https://doi.org/10.1207/S15324796ABM2602_07.

69. Dobin, A., Davis, C.A., Schlesinger, F., Drenkow, J., Zaleski, C., Jha, S., Batut, P., Chaisson, M., and Gingeras, T.R. (2013). STAR: ultrafast universal RNA-seq aligner. Bioinformatics *29*, 15–21. https://doi.org/10.1093/bioinformatics/bts635.

70. Kim, D., Paggi, J.M., Park, C., Bennett, C., and Salzberg, S.L. (2019). Graph-based genome alignment and genotyping with HISAT2 and HISAT-genotype. Nat. Biotechnol. *37*, 907–915. https://doi.org/10.1038/s41587-019-0201-4.

71. Love, M.I., Huber, W., and Anders, S. (2014). Moderated estimation of fold change and dispersion for RNA-seq data with DESeq2. Genome Biol. *15*, 550. https://doi.org/10.1186/s13059-014-0550-8.

72. Wu, T., Hu, E., Xu, S., Chen, M., Guo, P., Dai, Z., Feng, T., Zhou, L., Tang, W., Zhan, L., et al. (2021). clusterProfiler 4.0: A universal enrichment tool for interpreting omics data. Innovation (Camb.) *2*, 100141. https://doi.org/10.1016/j.xinn.2021.100141.

73. Yu, G., Wang, L.G., Han, Y., and He, Q.Y. (2012). clusterProfiler: an R package for comparing biological themes among gene clusters. Omics *16*, 284–287. https://doi.org/10.1089/omi.2011.0118.

74. Phipson, B., Sim, C.B., Porrello, E.R., Hewitt, A.W., Powell, J., and Oshlack, A. (2022). propeller: testing for differences in cell type proportions in single cell data. Bioinformatics *38*, 4720–4726. https://doi.org/10.1093/bioinformatics/btac582.

75. Bates, D., Mächler, M., Bolker, B., and Walker, S. (2015). Fitting Linear Mixed-Effects Models Using lme4. J. Stat. Software *67*, 1–48.

76. Kuznetsova, A., Brockhoff, P.B., and Christensen, R.H.B. (2017). lmerTest Package: Tests in Linear Mixed Effects Models. J. Stat. Softw. *82*, 1–22. https://doi.org/10.18637/jss.v082.i13.

77. Moore, J., Basurto-Lozada, D., Besson, S., Bogovic, J., Bragantini, J., Brown, E.M., Burel, J.M., Casas Moreno, X., de Medeiros, G., Diel, E.E., et al. (2023). OME-Zarr: a cloud-optimized bioimaging file format with international community support. Histochem. Cell Biol. *160*, 223–251. https://doi.org/10.1007/s00418-023-02209-1.

78. Serra, D., Mayr, U., Boni, A., Lukonin, I., Rempfler, M., Challet Meylan, L., Stadler, M.B., Strnad, P., Papasaikas, P., Vischi, D., et al. (2019). Self-organization and symmetry breaking in intestinal organoid development. Nature *569*, 66–72. https://doi.org/10.1038/s41586-019-1146-y.

79. van der Walt, S., Schönberger, J.L., Nunez-Iglesias, J., Boulogne, F., Warner, J.D., Yager, N., Gouillart, E., and Yu, T.; scikit-image contributors (2014). scikit-image: image processing in Python. PeerJ *2*, e453. https://doi.org/10.7717/peerj.453.

80. Tough, I.R., Forbes, S., Tolhurst, R., Ellis, M., Herzog, H., Bornstein, J.C., and Cox, H.M. (2011). Endogenous peptide YY and neuropeptide Y inhibit colonic ion transport, contractility and transit differentially via Y_1 and Y_2 receptors. Br. J. Pharmacol. *164*, 471–484. https://doi.org/10.1111/j.1476-5381.2011.01401.x.

81. Magness, S.T., Puthoff, B.J., Crissey, M.A., Dunn, J., Henning, S.J., Houchen, C., Kaddis, J.S., Kuo, C.J., Li, L., Lynch, J., et al. (2013). A multicenter study to standardize reporting and analyses of fluorescence-activated cell-sorted murine intestinal epithelial cells. Am. J. Physiol. Gastrointest. Liver Physiol. *305*, G542–G551. https://doi.org/10.1152/ajpgi.00481.2012.

82. Risso, D., Ngai, J., Speed, T.P., and Dudoit, S. (2014). Normalization of RNA-seq data using factor analysis of control genes or samples. Nat. Biotechnol. *32*, 896–902. https://doi.org/10.1038/nbt.2931.

83. Liao, Y., Smyth, G.K., and Shi, W. (2014). featureCounts: an efficient general purpose program for assigning sequence reads to genomic features. Bioinformatics *30*, 923–930. https://doi.org/10.1093/bioinformatics/btt656.

84. Hao, Y., Hao, S., Andersen-Nissen, E., Mauck, W.M., 3rd, Zheng, S., Butler, A., Lee, M.J., Wilk, A.J., Darby, C., Zager, M., et al. (2021). Integrated analysis of multimodal single-cell data. Cell *184*, 3573–3587.e29. https://doi.org/10.1016/j.cell.2021.04.048.

85. Hafemeister, C., and Satija, R. (2019). Normalization and variance stabilization of single-cell RNA-seq data using regularized negative binomial regression. Genome Biol. *20*, 296. https://doi.org/10.1186/s13059-019-1874-1.

86. Squair, J.W., Gautier, M., Kathe, C., Anderson, M.A., James, N.D., Hutson, T.H., Hudelle, R., Qaiser, T., Matson, K.J.E., Barraud, Q., et al. (2021). Confronting false discoveries in single-cell differential expression. Nat. Commun. *12*, 5692. https://doi.org/10.1038/s41467-021-25960-2.

87. Hao, Y., Stuart, T., Kowalski, M.H., Choudhary, S., Hoffman, P., Hartman, A., Srivastava, A., Molla, G., Madad, S., Fernandez-Granda, C., et al. (2024). Dictionary learning for integrative, multimodal and scalable single-cell analysis. Nat. Biotechnol. *42*, 293–304. https://doi.org/10.1038/s41587-023-01767-y.

88. Marconato, L., Palla, G., Yamauchi, K.A., Virshup, I., Heidari, E., Treis, T., Vierdag, W.M., Toth, M., Stockhaus, S., Shrestha, R.B., et al. (2025). SpatialData: an open and universal data framework for spatial omics. Nat. Methods *22*, 58–62. https://doi.org/10.1038/s41592-024-02212-x.

89. Lenth, R. (2024). emmeans: Estimated Marginal Means, aka Least-Squares Means. https://cran.r-project.org/web/packages/emmeans/emmeans.pdf.

90. Schindelin, J., Arganda-Carreras, I., Frise, E., Kaynig, V., Longair, M., Pietzsch, T., Preibisch, S., Rueden, C., Saalfeld, S., Schmid, B., et al. (2012). Fiji: an open-source platform for biological-image analysis. Nat. Methods *9*, 676–682. https://doi.org/10.1038/nmeth.2019.

91. Bankhead, P., Loughrey, M.B., Fernández, J.A., Dombrowski, Y., McArt, D.G., Dunne, P.D., McQuaid, S., Gray, R.T., Murray, L.J., Coleman, H.G., et al. (2017). QuPath: Open source software for digital pathology image analysis. Sci. Rep. *7*, 16878. https://doi.org/10.1038/s41598-017-17204-5.

92. Acs, B., Pelekanou, V., Bai, Y., Martinez-Morilla, S., Toki, M., Leung, S.C.Y., Nielsen, T.O., and Rimm, D.L. (2019). Ki67 reproducibility using digital image analysis: an inter-platform and inter-operator study. Lab. Invest. *99*, 107–117. https://doi.org/10.1038/s41374-018-0123-7.

93. Hein, A.L., Mukherjee, M., Talmon, G.A., Natarajan, S.K., Nordgren, T.M., Lyden, E., Hanson, C.K., Cox, J.L., Santiago-Pintado, A., Molani, M.A., et al. (2021). QuPath Digital Immunohistochemical Analysis of Placental Tissue. J. Pathol. Inform. *12*, 40. https://doi.org/10.4103/jpi.jpi_11_21.

STAR★METHODS

KEY RESOURCES TABLE

REAGENT or RESOURCE	SOURCE	IDENTIFIER
Antibodies		
Rabbit anti-Ki67	Abcam	Cat#ab15580; RRID:AB_443209
Rabbit anti-Cleaved Caspase-3 (Asp175) (D3E9)	Cell Signaling Technology	Cat#9579; RRID:AB_10897512
Rabbit anti-Cleaved Caspase-3 (Asp175)	Cell Signaling Technology	Cat#9661; RRID:AB_2341188
DISCOVERY OmniMap Anti-Rb HRP (RUO)	Roche	Cat#760-4311; RRID:AB_2811043
Goat anti-rabbit Alexa Fluor 488	Invitrogen	Cat#A-11008; RRID:AB_143165
Goat anti-rabbit Alexa Fluor 594	Invitrogen	Cat#A-11012; RRID:AB_2534079
Alexa Fluor 647 anti-mouse EpCAM	BioLegend	Cat#118212; RRID:AB_1134104
PE anti-mouse CD45	BioLegend	Cat#103106; RRID:AB_312971
PE anti-mouse CD31	BioLegend	Cat#102408; RRID:AB_312902
PE anti-mouse TER-119	BioLegend	Cat#116208; RRID:AB_313708
Mouse anti-PCNA (PC10)	Cell Signaling Technology	Cat#2586; RRID:AB_2160343
Rat anti-CD44v6 (9A4)	Bio-Rad	Cat#MCA1967; RRID:AB_323213
Bacterial and virus strains		
Lactiplantibacillus plantarum WJL strain (Lp^{WJL})	Neobiosys	Batch LPWJL220421-Actif
Chemicals, peptides, and recombinant proteins		
5-Ethynyl-2′-deoxyuridine (EdU)	Santa Cruz Biotechnology	Cat#sc-284628
Formaldehyde solution phosphate buffered (10% NBF)	Fisher Scientific	Cat#F/1520/21
Paraformaldehyde (PFA)	Sigma-Aldrich	Cat#158127
DISCOVERY CC1 Solution	Roche	Cat#950-500
O.C.T. Compound	VWR	Cat#361603E
VECTASHIELD Antifade Mounting Medium with DAPI	Vector Laboratories	Cat#H-1200-10
ProLong Gold Antifade Mountant	Invitrogen	Cat#P36934
Epitope Retrieval Solution 2 (pH6)	Leica Biosystems	Cat#AR9640
OPAL 570	Akoya Biosciences	Cat#FP1488001KT
OPAL 690	Akoya Biosciences	Cat#FP1497001KT
OPAL 780	Akoya Biosciences	Cat#FP1501001KT
Novolink Polymer Detection Systems	Leica Biosystems	Cat#RE7260-CE
TRIzol Reagent	Invitrogen	Cat#15596026
Dulbecco's Phosphate Buffered Saline (DPBS)	Gibco	Cat#14190250
Hanks' Balanced Salt Solution (HBSS)	Gibco	Cat#14175129
Dulbecco's Modified Eagle Medium/ Nutrient Mixture F-12 (DMEM/F-12)	Gibco	Cat#21041025
UltraPure 0.5M EDTA, pH 8.0	Invitrogen	Cat#15575020
HEPES solution	Sigma-Aldrich	Cat#H0887
DTT	Roche	Cat#DTT-RO
Fetal Bovine Serum	Sigma-Aldrich	Cat#F9665
Collagenase/Dispase	Roche	Cat#COLLDISP-RO
DNase I	Roche	Cat#11284932001
Trypan Blue	Gibco	Cat#15250061
DAPI	BD Pharmingen	Cat#564907

(*Continued on next page*)

Continued

REAGENT or RESOURCE	SOURCE	IDENTIFIER
D-(+)-Glucose	Sigma-Aldrich	Cat#G8270
D-(−)-Fructose	Sigma-Aldrich	Cat#F0127
Sodium Chloride	Sigma-Aldrich	Cat#S7653
Sucrose	Sigma-Aldrich	Cat#S1888
DAPI	Thermo Scientific	Cat#62248
Matrigel, Growth Factor Reduced	Corning	Cat#356231
DMEM/F-12 with 15 mM HEPES	STEM CELL Technologies	Cat#36254
Penicillin and Streptomycin	VWR	Cat#392-0406
GlutaMAX Supplement	Gibco	Cat#35050061
B-27 Supplement	Gibco	Cat#17504001
N-2 Supplement	Gibco	Cat#17502048
N-Acetyl-L-cysteine	Sigma-Aldrich	Cat#A7250
R-Spondin	Novartis	N/A
Mouse Noggin Recombinant Protein	Gibco	Cat#250-38
Mouse EGF Recombinant Protein	R&D Systems	Cat#2028-EG-200
Paraformaldehyde 16% Aqueous Solution	Electron Microscopy Sciences	Cat#15710-S
Normal Donkey Serum	Sigma-Aldrich	Cat#S30-M
Mouse Prolactin Recombinant Protein	Gibco	Cat#315-16
Critical commercial assays		
Click-iT Plus EdU Cell Proliferation Kit for Imaging, Alexa Fluor 488 dye	Invitrogen	Cat#C10637
Click-iT Plus EdU Cell Proliferation Kit for Imaging, Alexa Fluor 647 dye	Invitrogen	Cat#C10640
DISCOVERY ChromoMap DAB Kit (RUO)	Roche	Cat#760-159
DeadEnd Colorimetric TUNEL System Kit	Promega	Cat#G7130
RNAscope LS Multiplex Fluorescent Assay	Bio-Techne	Cat#322800
RNeasy Plus Micro Kit	Qiagen	Cat#74034
RNeasy Plus Mini Kit	Qiagen	Cat#74134
RNeasy Mini Kit	Qiagen	Cat#74104
SuperScript VILO Master Mix	Invitrogen	Cat#11766050
TaqMan Gene Expression Master Mix	Applied Biosystems	Cat#4369510
T7 mMessage mMachine Kit	Invitrogen	Cat#AM1344
NEBNext Ultra II Directional RNA Library Prep Kit for Illumina	New England Biolabs	Cat#E7760
NEBNext Poly(A) mRNA Magnetic Isolation Module	New England Biolabs	Cat#E7490
Chromium Next GEM Single Cell 3' GEM, Library & Gel Bead Kit v3.1	10x Genomics	Cat#1000121
Xenium *In Situ* Gene Expression with Cell Segmentation Kits	10x Genomics	Cat#1000460; Cat#1000487; Cat#1000661
Deposited data		
Small intestine bulk RNA sequencing	This paper	GEO: GSE247929, GSE247926
FACS-sorted intestinal epithelium bulk RNA sequencing, lactating	This paper	GEO: GSE247929, GSE247923
FACS-sorted intestinal epithelium bulk RNA sequencing, pregnancy	This paper	GEO: GSE247929, GSE247925
FACS-sorted intestinal epithelium single-cell RNA sequencing	This paper	GEO: GSE247929, GSE247927
Gut rolls Xenium *in situ* spatial imaging analysis	This paper	GEO: GSE285027

(*Continued on next page*)

Continued

REAGENT or RESOURCE	SOURCE	IDENTIFIER
Mendeley Data	This paper	Mendeley Data: https://doi.org/10.17632/f239gwztnm.1
Experimental models: Organisms/strains		
Mouse: C57BL/6J wildtype mice	The Jackson Laboratory	RRID:IMSR_JAX:000664
Mouse: SGLT3a/3b double knockout: C57BL/6N-Del(10Slc5a4a-Slc5a4b)Csk	Riken	BRC No. RBRC06158
Mouse: SGLT3a single knockout: C57BL/6N-Slc5a4a<tm1Csk>	Riken	BRC No. RBRC06156
Oligonucleotides		
RNAscope Mm-*Slc5a4a* probe	Bio-Techne	Cat#462288
RNAscope Mm-*Lgr5* probe	Bio-Techne	Cat#312178
RNAscope Mm-*Fgfbp1* probe	Bio-Techne	Cat#508838
RNAscope Mm-*Ada* probe	Bio-Techne	Cat#562508
RNAscope Mm-*Slc2a2*-E11 probe	Bio-Techne	Cat#439898
RNAscope Mm-*Krt19* probe	Bio-Techne	Cat#402948
TaqMan Mm-*Slc5a4a* probe	Applied Biosystems	Cat# Mm01173149_m1
TaqMan Mm-*Slc5a4b* probe	Applied Biosystems	Cat# Mm01173529_m1
TaqMan Mm-*Slc5a1* probe	Applied Biosystems	Cat# Mm00451203_m1
TaqMan Mm-*Slc2a2* probe	Applied Biosystems	Cat# Mm00446229_m1
TaqMan Mm-*Slc2a5* probe	Applied Biosystems	Cat# Mm00600311_m1
TaqMan Mm-*Sis* probe	Applied Biosystems	Cat# Mm01210305_m1
TaqMan Mm-*Mgam* probe	Applied Biosystems	Cat# Mm01163791_m1
TaqMan Mm-*Gapdh* probe	Applied Biosystems	Cat# Mm03302249_g1
TaqMan Mm-*Actb* probe	Applied Biosystems	Cat# Mm02619580_g1
Recombinant DNA		
pUNIV-mSGLT3a (*Slc5a4a*)	This paper	N/A
pUNIV-mSGLT3b (*Slc5a4b*)	This paper	N/A
pUNIV-mSGLT1 (*Slc5a1*)	This paper	N/A
Software and algorithms		
FACSDiva v9.0.1	BD Biosciences	RRID:SCR_001456
FlowJo v10.8.1	BD Biosciences	RRID:SCR_008520
Fiji (imageJ) v2.3.0	National Institutes of Health	RRID:SCR_002285
QuPath v0.3.2	https://qupath.github.io	RRID:SCR_018257
R v4.3.1	R Core Team	RRID:SCR_001905
RStudio	RStudio	RRID:SCR_000432
pCLAMP with ClampFit Software	Molecular Devices	RRID:SCR_011323
GraphPad Prism v10.1.1	GraphPad Software	RRID:SCR_002798
Adobe Illustrator	Adobe	RRID: SCR_010279
FastQC v0.11.5	http://www.bioinformatics.babraham.ac.uk/projects/fastqc/	RRID:SCR_014583
STAR v2.7.7a	Dobin et al.[69]	RRID:SCR_004463
HISAT2 v2.0.4	Kim et al.[70]	RRID:SCR_015530
DESeq2 v1.34.0	Love et al.[71]	RRID:SCR_015687
clusterProfiler v4.8.3	Wu et al.[72]; Yu et al.[73]	RRID:SCR_016884
CellRanger v5.0.1	10x Genomics	RRID:SCR_017344
Seurat v4.3.0.1	Satija Lab	RRID:SCR_016341
speckle v1.4.0	Phipson et al.[74]	https://www.bioconductor.org/packages/release/bioc/html/speckle.html
lme4 v1.1.35	Bates et al.[75]	RRID:SCR_015654

(*Continued on next page*)

Continued

REAGENT or RESOURCE	SOURCE	IDENTIFIER
lmerTest v3.1.3	Kuznetsova et al.[76]	RRID:SCR_015656
Other		
Axio Scan Z1 Slide Scanner	Zeiss Microscopy	N/A
Akoya PhenoImager HT (formerly Vectra Polaris)	Akoya Biosciences	N/A
Leica Stellaris 5 Confocal Microscope	Leica Microsystems	N/A
Leica SP5 II Confocal Microscope	Leica Microsystems	N/A
BD FACSAria III Cell Sorter	BD Biosciences	N/A
EchoMRI-100H	EchoMRI	N/A
BioDAQ System	Research Diets	N/A
Contour Next Blood Glucose Meter	Contour	N/A
Contour Next Blood Glucose Test Strip	Contour	N/A
6725 Semimicro Calorimeter	Parr Instruments	N/A
6772 Calorimetric Thermometer	Parr Instruments	N/A
Oocyte Clamp OC-725C amplifier	Warner Instruments	N/A
Nextseq550	Illumina	N/A
NextSeq2000	Illumina	N/A
10x Xenium Analyser	10x Genomics	N/A
Cell Voyager 7000S and 8000	Yokogawa	N/A

EXPERIMENTAL MODEL AND STUDY PARTICIPANT DETAILS

Mice

Strains

All mouse experiments were performed in accordance with the UK Animals (Scientific Procedures) Act 1986. 7–10-week-old C57BL/6J wild-type mice were purchased from Charles River, UK. SGLT3 double knockout (*Slc5a4a*$^{-/-}$, *Slc5a4b*$^{-/-}$) and SGLT3a single knockout (*Slc5a4a*$^{-/-}$) mice were re-derived from purchased cryopreserved sperm from C57BL/6N-Del (10Slc5a4a-Slc5a4b)Csk (Riken, RBRC06158) and C57BL/6N-Slc5a4a<tm1Csk> (Riken, RBRC06156) mice, respectively. SGLT3 double and SGLT3a single knockout mice were bred and maintained at the animal facilities of Imperial College London, UK. Mice were housed under specific-pathogen-free conditions on a 12 h dark/light cycle at constant temperature (20–22°C) and humidity (45–50%). Experimental repeats were conducted at comparable times to minimise possible circadian effects.

Breeding

Age-matched groups of littermates were used for all experiments. For the experimental breeding, 8–15-week-old females were used for mating with males. For pregnancy and lactation experiments, pregnancy day 0 was defined by detection of a vaginal plug; lactation day 0 was defined by the birth of pups; post-lactating day 0 was defined by removal of pups at lactation day 7. Pseudopregnancy was defined by detection of a vaginal plug after mating with vasectomised males. For the pseudopregnancy experiments, pregnancy day 7 (D7) and pseudopregnancy day 7 (D7) were used as time points for pregnancy and pseudopregnancy, respectively.

For all experiments using lactating knockout mice, we used only dams with a litter size of 4 or more at lactation day 7, where we confirmed that the number pups were comparable between lactating control and KO mice within the experimental batch.

Diets

Mice were fed a standard diet whilst breeding or in maintenance colonies at the animal facilities of Imperial College London, UK: RM3 during breeding and RM1 for maintenance and experiments (Special Diets Services). We did not see any effects of the difference between RM1 and RM3 diet on the maternal small intestine length.

For the high-fructose corn syrup (HFCS) experiment, HFCS was prepared by combining D-(+)-glucose (Sigma-Aldrich, G8270) and D-(−)-fructose (Sigma-Aldrich, F0127) in a 45:55 ratio as previously described.[61] Age-matched virgin females were provided with either *ad libitum* 25% HFCS or H_2O control drinking water, and had free access to RM1 diet for the duration of the experiment (EchoMRI body composition measurements at 4 weeks and tissue harvesting at 6 weeks).

For the high salt diet (HSaD) experiment, age-matched virgin females were provided with either *ad libitum* 1% NaCl water or H2O control drinking water, and had free access to isocaloric 0.49% NaCl diet (Envigo, TD.96208) or 4% NaCl diet (Envigo, TD.92034), respectively for 1 week.

For daily food intake measurement, experimental female mice were singly-housed and food was weighed every 24 h or monitored by BioDAQ system (Research Diets).

Germ-free mice

Germ-free (GF) and specific pathogen-free (SPF) C57BL/6J mice were bred in the Laboratory of Gnotobiology, Institute of Microbiology, Czech Republic, for more than 10 generations. GF mice were housed in Trexler-type plastic isolators, exposed to a 12:12 hour light:dark cycle and supplied with autoclaved tap water and 50 kGy irradiated (Bioster, Czech Republic) sterile mouse breeding diet V1124-300 (Ssniff Spezialdiäten, Germany) ad libitum. The mice were bred on sterile SAFE select fine bedding irradiated with 50 kGy (Safe, Rosenberg, Germany) with enrichment nestlets (Plexx, Anlab, Czech Republic). Axenicity was assessed every third week as previously described.[46] Briefly, the absence of bacteria, molds, and yeasts was assessed by aerobic and anaerobic cultivation of mouse feces and swabs from the isolators. In addition, weekly Gram staining of fecal smears and inspection under the microscope were performed. SPF control C57Bl/6J mice were housed in a 12-hour light-dark cycle with free access to water and fed ad libitum with 25 kGy irradiated sterile mouse breeding diet V1124-300 (Ssniff Spezialdiäten, Germany) in individually ventilated cages (IVC, Tecniplast, Italy). Ten-week-old females from at least 2 litters were mated or kept as virgins. After birth, the pups were counted and at the time of lactation D7, the mothers were weighed and euthanized together with the pups by cervical dislocation between 10 and 11 a.m. The small intestines of the mothers were removed, weighed and the length was measured, and samples of the duodenum, jejunum and ileum were taken. The animal experiments were approved by the Committee for the Protection and Use of Experimental Animals of the Institute of Microbiology of the Czech Academy of Sciences (approval ID: 56/2021).

Probiotics supplementation

Specific pathogen-free male and female C57Bl/6J mice (9–10-week-old) were obtained from Charles River (L'Arbresle, France). The mice were housed in Innorack IVC Mouse 3.5 disposable cages (Inovive, USA) under a 12:12-hour light-dark cycle, with *ad libitum* access to tap water and food (Altromin 1310) in conventional animal house, IGFL, France. All procedures were conducted in compliance with the European Community Council Directive of September 22, 2010 (2010/63/EU) concerning the protection of animals used for scientific and experimental purposes. After a one-week acclimatization period, the mice were mated. Females identified as mated by the presence of a vaginal plug were isolated. Control (non-mated) females were housed in groups of one to six per cage. On the day of delivery, the pups were counted, and when they reached seven days of age, the mothers and pups were weighed and euthanized by cervical dislocation. The mothers' small intestines were collected, weighed, and measured, and samples of the duodenum, jejunum, and ileum were taken. Mothers were treated daily, five days per week, from the day of plug detection until the day of euthanasia. Control females (non-mated) received identical treatment schedules. The treatment consisted of administering either a placebo solution (maltodextrin) or a solution containing 10^8 CFU of *Lactiplantibacillus plantarum* WJL (Lp^{WJL}) dissolved in maltodextrin. A 100 μL dose of the experimental solutions was delivered using a pipette, gently in the hollow of the cheek.

Mouse intestinal organoids

Maintenance of organoids

Organoids from female wild-type C57BL/6J mice or $SGLT3a^{KO}$ were cultured in ENR medium: DMEM/F-12, 15 mM HEPES (STEM CELL Technologies, 36254) supplemented with 100 μg/ml Penicillin and Streptomycin, 1x Glutamax (Gibco, 35050061), 1x B27 (Gibco, 17504001), 1x N2 (Gibco, 17502048), 1 mM N-acetylcysteine (Sigma, A7250), 500 ng/ml R-Spondin (kind gift from Novartis), 100 ng/ml Noggin (Gibco, 250-38) and 100 ng/ml murine EGF (R&D Systems, 2028-EG-200). For maintenance, organoids were hard split every 4–5 days, as following: medium was removed and organoids collected in DMEM/F-12, Pen/Strep and Glutamax. After pelleting at 600g for 5 min at 4°C, ENR medium was added and organoids were hard-split by pipetting up and down for 30 times. Organoids were plated in 50% ENR and 50% Matrigel (Corning, 356231). After 30 min of solidification at 37°C, ENR medium was added.

Time course experiment

To assess organoid growth of the different lines, organoids were collected as described above and hard-split by pipetting up and down for 40x. Organoids were collected in 50% ENR and 50% Matrigel (Corning, 356231) and 5 μl droplets were plated into 96-well plates (Greiner). After 15 min of solidification at 37°C, ENR medium was added. 24 h after plating, EdU pulse of 30 min was performed using Click-iT Plus EdU Cell Proliferation Kit (Invitrogen, C10640), according to the manufacturer's instructions. At 48 h post plating, organoids were fixed in 4% PFA (Electron Microscopy Sciences, 15710-S) in PBS for 45 min at room temperature. After washing three times with PBS, antibody staining procedure was performed. For PCNA stainings, permeabilization was performed by incubation in methanol for 30 min at -20°C. For EdU detection experiments, permeabilization was performed using 0.5% Triton X-100 (Sigma) for 1 h followed by EdU detection procedure (according to the manufacturer's instructions). The samples were blocked for 1 h with 3% Normal Donkey Serum (Sigma, S30-M) in PBS with 0.1% Triton X-100 (Sigma) at room temperature. Primary antibody staining was performed in blocking buffer overnight at 4°C and followed by secondary antibody staining for 2 h at room temperature.

Imaging and image analysis

High-throughput imaging of mouse intestinal organoids was performed using a Yokogawa CellVoyager, 7000S and 8000, equipped with CSU-W1 Confocal Scanner Unit and a 20x/0.75 Air objective. Z-stacks of around 100 μm were acquired at a z-step of 5 μm. Raw

images were processed using the Fractal platform (https://fractal-analytics-platform.github.io/).[77] Organoid segmentation was performed using a RDCnet network based on DAPI trained organoid data).[78] Organoid-level segmentations were manually corrected and automated feature extraction was performed using the scikit-image package.[79] Mean intensities were normalized to the mean intensity of the wild-type control within each experiment.

RT-qPCR

Organoids from 2-wells of a 24-well plate were collected after 48 h of prolactin (Recombinant Murine Prolactin, Gibco, 315-16) treatment. Medium containing prolactin was refreshed every at 24 h and RNA was extracted using the RNeasy Kits for RNA Purification (Qiagen, 74104) kit including the DNAse I step. cDNA was synthesized using the SuperScript VILO Master Mix (Invitrogen, 11766050). For gene expression analysis, real-time RT-PCR was performed using TaqMan probes (Thermo Fisher Scientific), and TaqMan Gene Expression Master Mix (Applied Biosystems, 4369510). The following probes were used: Mm01173149_m1, *Slc5a4a*; Mm01173529_m1, *Slc5a4b*; Mm03302249_g1, *Gapdh*.

METHOD DETAILS

Metabolic measurements

Body composition (fat and lean mass) was assessed using an EchoMRI-100H (EchoMRI) device in restrained, conscious mice. The machine was calibrated using a canola oil standard prior to each session.

For the oral glucose tolerance test, mice were fasted overnight (approximately 16 h) prior to the glucose tolerance test (GTT) by placing them into a fresh cage with free access to water. Mice received an oral gavage of 1 mg glucose (Sigma, G8270) per body weight (g). Blood glucose from the tail was measured using a glucometer (Contour) before the oral gavage (0 min) and 15, 30, 60, 90, and 120 min post-oral gavage.

Bomb calorimetry

Faeces samples were freshly collected and desiccated in a drying oven (60°C for 4 days). Approximately, 200 mg of dried stool was pressed into a pellet using a pellet press (Parr Instruments). Gross energy content was measured using a semimicro oxygen bomb calorimeter (Parr Instruments, 6725) and calorimetric thermometer (Parr Instruments, 6772). The calorimeter energy equivalent factor was determined using benzoic acids standards. Calorie consumed from diet was calculated by multiplying caloric density of food and daily food intake. Calorie lost in faeces was calculated by multiplying caloric density of faeces and daily faeces amount. Calorie absorbed from diet was calculated by subtracting calorie lost in faeces from calorie consumed from diet. Digestive efficiency was calculated by dividing calorie absorbed by calorie consumed from diet.

Immunohistochemistry (IHC)

Tissue was fixed for 24 h in 10% Neutral Buffered Formalin (NBF) before processing to wax using a Tissue-Tek VIP 6 AI processor. 3 μm tissue sections baked for 1 h at 60°C prior to immunohistochemical staining using on a Roche Ventana Discovery Ultra autostainer for rabbit anti-Ki67 antibody (1:3000, Abcam, ab15580) or rabbit anti-Cleaved Caspase-3 (1:250, Cell Signaling Technology, 9579S) with DISCOVERY OmniMap anti-Rb HRP (RUO) (Roche, 760-4311) and detected with DISCOVERY ChromoMap DAB Kit (RUO) (Roche, 760-159). DISCOVERY CC1 solution (Roche, 950-500) was used to retrieve the targets. Slides were counterstained with haematoxylin using a Tissue-Tek Prisma automated slide stainer. Slides were coverslipped using Tissue-Tek Glas g2 Automated Glass Coverslipper. Terminal deoxynucleotidyl transferase dUTP nick end labeling (TUNEL) assay for detecting DNA fragments (apoptosis) was performed on paraffin-embedded sections with DeadEnd Colorimetric TUNEL System kit (Promega, G7130), following manufacturer's instructions.

Immunofluorescence (IF)

Immunofluorescence was performed on PFA-fixed frozen sections. Small intestine pieces were fixed with 4% paraformaldehyde for 24 h at 4°C. Tissue was cryopreserved after 30% sucrose incubation overnight, embedded in a OCT mounting media (VWR, 361603E) and sectioned at 14 μm. Sections were permeabilised (0.3% PBS-Triton) for 10 min, blocked (10% goat serum in 0.3% PBS-Triton) for 30 min and incubated with primary antibodies overnight at 4°C. Sections were washed in 0.3% PBS-Triton, and incubated with secondary antibodies in blocking solution for 2 h at room temperature, washed and mounted with VECTASHIELD Antifade Mounting Medium with DAPI (Vector Laboratories, H-1200). Primary antibodies used were rabbit anti-Ki67 (1:200, abcam, ab15580) and rabbit anti-Cleaved Caspase-3 (1:200, Cell Signaling Technologies, 9661). Secondary antibodies used were goat anti-rabbit Alexa Fluor 488 (1:800, Invitrogen, A-11008) and goat anti-rabbit Alexa Fluor 594 (1:500, Invitrogen, A-11012).

For EdU tracing experiments, EdU (100 mg/kg, Santa Cruz Biotechnology, sc-284628) was dissolved in sterile PBS was injected intraperitoneally 24 h before mouse euthanasia. EdU staining was performed using the Click-iT Plus EdU Cell Proliferation Kit, Alexa Fluor 488 (Invitrogen, C10637) according to the manufacturer's instructions.

Single molecule fluorescence in situ hybridization (smFISH)

Multiplex RNAscope was performed using Leica Bond Rx automated stainer. Tissue was fixed for 24 h in 10% NBF before processing to wax using a Tissue-Tek VIP 6 AI processor. 5 μm FFPE sections were baked for 1 h at 60°C and stained on the Leica Bond Rx

automated stainer using RNAscope LS Multiplex Fluorescent assay (ACD Bio-Techne, 322800). Epitope Retrieval Solution 2 (pH6) (Leica, AR9640) was applied for 15 min at 88°C for target retrieval and 15 min protease treatment was performed using target probes detected with Opal 570 (1:1000, Akoya, FP1488001KT), Opal 690 (1:1000, Akoya, FP1497001KT) or Opal 780 (1:100 and 1:25, Akoya, FP1501001KT). Target probes used were Mm-Slc5a4a (462288); Mm-Lgr5 (312178); Mm-Fgfbp1 (508838); Mm-Ada (562508); Mm-Slc2a2-E11 (439898); Mm-Krt19 (402948), purchased from Bio-Techne. For the co-staining of Slc5a4a FISH and anti-Ki67 IF, samples were also immunostained with anti-rabbit Ki67 antibody (1:2500, Abcam, ab15580) and anti-rabbit Poly-HRP-IgG (Leica, Novolink Max Polymer, RE7260-CE) detected with Opal 570 (1:500, Akoya, FP1488001KT). Slides were counterstained with DAPI (Thermo Scientific, 62248) 1:2500 and mounted with Prolong Gold Antifade reagent (Invitrogen, P36934). Slides were scanned using the Akoya PhenoImager HT (formerly Vectra Polaris) using MOTiF scanning mode.

RNA extraction and quantitative RT-PCR

For tissue, RNA was isolated using the TRIzol (Invitrogen, 15596026) according to the manufacturer's protocol. For FACS-sorted cells, RNA was isolated using the RNeasy Plus Micro kit (Qiagen, 74034) according to the manufacturer's protocol. cDNA was synthesized using the SuperScript VILO Master Mix (Invitrogen, 11766050). For gene expression analysis, real-time RT-PCR was performed using TaqMan probes (Thermo Fisher Scientific), and TaqMan Gene Expression Master Mix (Applied Biosystems, 4369510). The following probes were used: Mm01173149_m1, *Slc5a4a*; Mm01173529_m1, *Slc5a4b*, Mm00451203_m1, *Slc5a1*; Mm00446229_m1, *Slc2a2*; Mm00600311_m1, *Slc2a5*; Mm01210305_m1, *Sis*; Mm01163791_m1, *Mgam*; Mm03302249_g1, *Gapdh*; Mm02619580_g1, *Actb*.

Electrophysiology assay in *Xenopus* oocytes

Full-length mSGLT3a, mSGLT3b, and SGLT1 cDNA was synthesized and cloned into pUNIV vector by Genewiz. cRNA was prepared from linearised DNA plasmid (2 h digestion with NotI restriction enzyme) followed by cRNA synthesis using the T7 mMessage mMachine kit (Invitrogen, AM1344). *Xenopus laevis* oocytes were injected with 25–50 nL of cRNA (1000–1,500 ng/uL) and incubated at 18°C for 2–4 days for transporter expression. Transporter currents were measured by two-electrode voltage clamp technique at room temperature. Oocytes were continuously perfused with ND96 recording solution at pH 7.5 (baseline conditions) and treatments were prepared with the same solution modifying only pH or sugar concentration. Na^+-free and Na^+ dose-response solutions were prepared by replacing Na^+ with $NMDG^+$ to balance solution osmolarity (~180-200 mOsm). Cl^- free solutions used equimolar gluconate substitution. Transporter currents were amplified and measured using Oocyte Clamp OC-725C amplifier (Warner Instruments), digitized with Digidata 1550B (Axon Instruments), and recorded using pCLAMP v11.2 (Molecular Devices).

Mucosal preparation and Ussing chamber electrophysiology

Ileum (4 cm) was excised 4 cm proximal to the ileocaecal junction from age-matched female virgin control, lactating control, or lactating $SGLT3^{KO}$ mice. Eight adjacent ileal mucosae were prepared by dissecting both longitudinal and circular smooth muscle layers and associated myenteric plexi, from the underlying mucosa with its intact submucosal innervation. Each mucosal preparation was then placed in an Ussing chamber, bathed both sides in Krebs-Henseleit (containing, in mM: NaCl 118, KCl 4.7, $NaHCO_3$ 25, KH_2PO_4 1.2, $MgSO_4$ 1.2, $CaCl_2$ 2.5, glucose 11.1 at pH 7.4) at 37°C, gassed with 95% O_2/5% CO_2, and voltage-clamped at 0 mV as described previously.[80] The resulting basal short-circuit current (I_{sc}) was allowed to equilibrate (20–30 min) and the transepithelial resistance (TER) was measured by applying a ±0.5 mV step (for 5 sec every 2 min, measuring consequent I_{sc} deflections and applying Ohm's law) throughout the equilibration period. The basal I_{sc} and TER values were captured upon equilibration, and these measurements were transformed to cm^2 areas. Values were pooled and expressed as the mean ± 1SEM.

Isolation of intestinal epithelium

Epithelial isolation and dissociation were performed as previously described[81] with some modifications. The posterior part of small intestine (ileum) corresponding to a 10 cm region from 2 to 12 cm distal to the caecum was isolated, cut open longitudinally, and rinsed with ice-cold Dulbecco's phosphate buffered saline (DPBS, Gibco, 14190250) to remove luminal contents. The intestinal tissue was incubated in dissociation reagent, first in DPBS containing 30 mM EDTA (Invitrogen, 15575020), 1.5 mM DTT (Roche, DTT-RO) on ice for 20 min, and then in DPBS containing 30mM EDTA at 37°C for 8 min, then shaken by hand for 20–30 sec to collect crypt/villus units. The cells were pelleted at 300g for 2 min at 4°C, washed once in DPBS containing 10% fetal bovine serum (FBS, Sigma-Aldrich, F9665), and pelleted again. Cells were incubated in Hanks' balanced salt solution (HBSS, Gibco, 14175129) containing 1 mg/mL of collagenase/dispase (Roche, COLLDISP-RO) at 37°C for 10 min, with intermittent shaking for 15 sec every 2 min to dissociate epithelial sheets into single cells. To enhance cell viability and decrease cell clumping, FBS and DNase I (Roche, 11284932001) were added to the cell suspension, which was sequentially filtered through cell strainers with 70 μm and then 40 μm filters (BD Falcon, 352350 and 352340, respectively). Cells were pelleted, washed in HBSS containing 10% FBS, re-pelleted and re-suspended in FACS buffer, which is composed of DMEM/F-12 (Gibco, 21041025), 25 mM HEPES (Sigma-Aldrich, H0887), and 2% FBS. Cell viability was assessed by Trypan blue (Gibco, 15250061).

Flow cytometry

To isolate EpCAM+ intestinal epithelium, single-cell suspensions prepared as above. Approximately 2.25 x 10^6 cells in 225 μL of FACS buffer (DMEM/F-12 containing 2% FCS) were stained with 4 antibodies (9 μL of Alexa Fluor 647 anti-mouse EpCAM, BioLegend, 118212; 4 μL of PE anti-mouse CD45, BioLegend, 103106; 4 μL of PE anti-mouse CD31, BioLegend, 102408; and 4 μL of PE anti-mouse TER-119, BioLegend, 116208 at 4°C for 10 min. DAPI (BD Pharmingen 564907) was added to the FACS buffer for 10 min before FACS sorting to eliminate dead/dying cells. EpCAM+ and CD45-/CD31-/TER-119- (to exclude lymphocytes, endothelial cells, and erythroid cells, respectively) cells were sorted on a FACS Aria III (BD) equipped with 488 nm, 405 nm, 561 nm and 633 nm lasers. Forward and side scatter measurements were made using the 488 nm laser, and doublets were excluded using forward scatter area vs forward scatter height and side scatter area vs side scatter height. DAPI was excited with the 405 nm laser and emission was measured using a 450/50 band pass filter. PE was excited using the 561 nm laser and emission was measured using a 582/15 band pass filter. Alexa Fluor 647 was excited using the 633 nm laser and emission was measured using a 660/20 bandpass filter. Data was analysed using FACS Diva (BD, Version 9.0.1) and FlowJo (BD Version 10.8.1).

Bulk RNA sequencing

Small intestine

RNA was harvested using TRIzol (Invitrogen, 15596026) and RNeasy Plus Mini Kit (Qiagen, 74134) according to the manufacturer's protocol. 200 ng of total RNA was used for the construction of sequencing libraries. RNA libraries were prepared using NEBNext Ultra II Directional RNA library prep kit with the NEBNext PolyA Enrichment module following the manufacturer's protocols. Libraries were sequenced on a Nextseq550 using paired-end 75bp reads. Sequenced samples (duodenum, jejunum and ileum) were quality controlled using FastQC (https://www.bioinformatics.babraham.ac.uk/projects/fastqc/), followed by alignment to the mouse genome (GRCm38 with Ensembl v84 annotations) and gene-based counting using STAR (v2.7.7a).[69] Data normalisation and differential expression analysis were conducted in R using the Bioconductor package DESeq2 (v1.34.0).[71] To ensure data reliability, additional quality assessments were performed, including PCA and hierarchical clustering, prior to analysis of differential expression using the Wald test. Differentially expressed genes were defined by using adjusted p-value < 0.05 after multiple testing correction with the Benjamini-Hochberg method. Where samples were collected and sequenced separately, contributions from this potential confounding factor were removed by batch correction using the RUVgseq (estimating the factors of unwanted variation using empirical control genes) function from the RUVseq R bioconductor package with k=3.[82] Gene ontology (GO) enrichment analysis was performed using the clusterProfiler R package v4.8.3,[72,73] using a padj < 0.05 cutoff for differentially expressed genes. The gene-concept network plot was visualised using the cnetplot function from the enrichplot R package v1.20.3 (https://bioconductor.org/packages/release/bioc/html/enrichplot.html).

FACS-sorted intestinal epithelium

RNA was harvested using RNeasy Plus Micro Kit (Qiagen, 74034) according to the manufacturer's protocol. 200 ng of total RNA was used for the construction of sequencing libraries. RNA libraries were prepared using NEBNext Ultra II Directional RNA library prep kit with the NEBNext PolyA Enrichment module following the manufacturer's protocols. Sequenced samples were quality controlled using FastQC v0.11.5 and aligned using HISAT2 v2.0.4[70] to the mouse genome (GRCm38 with Ensembl v84 annotations). Gene-based read counts were then obtained using the featureCounts function from the Rsubread Bioconductor package (v.1.24.2),[83] with arguments isPairedEnd=TRUE, strandSpecific=2. Data normalisation and analysis of differential expression was performed within R Bioconductor package DESeq2 (v1.24.0).[71] Samples were further quality assessed by principal component analysis (PCA) and hierarchal clustering, as well as by comparison to an expression matrix corrected for sample collection. Statistical testing was performed using the Wald test using the design '~Group+Batch' to allow for any small contributions from this confounding factor. Differentially expressed genes were defined by an adjusted p-value < 0.05 after multiple testing correction with the Benjamini-Hochberg method.

Single-cell RNA sequencing

For each sample, a library was generated from individual cells using the 10x Genomics Chromium Controller microfluidics system and the 3' v3.1 chemistry. Subsequent sequencing was performed on an Illumina NextSeq 2000 instrument with recommended settings.

10x Genomics CellRanger v5.0.1 was used for barcode splitting, unique molecular identifier (UMI) counting, and aligning sequences to the mouse genome (GRCm38, Ensembl 107 annotations). Quality control and subsequent analyses were carried out using Seurat v4.3.0.1[84] in R. Following recommendations, cells with low UMI counts (<500), low feature counts (<100), or high fractions of mitochondrial DNA (>25%) were excluded.

Samples were normalised using the sctransform method within Seurat[85] and were integrated based on the 3000 anchors selected using the FindIntegrationFeatures function. The effectiveness of this integration was verified by assessing the uniformity of cells across the combined UMAP space. Clusters were identified using the FindClusters function using a resolution of 0.6 to yield larger numbers of communities than the default.

Cell type annotation

Marker expression analysis was performed using the FindMarkers function from Seurat R package using the Wilcoxon Rank Sum test. Cell types were annotated based on the expression of known marker genes (as shown in Figure 4D).[48] Briefly, we annotated

Lgr5+ CBCs, *Lyz1*+ Paneth cells, *Fgfbp1*+*Mki67*+ isthmus progenitors, *Muc2*+ goblet cells, *Chgb*+ enteroendocrine cells, *Atoh1*+ secretory progenitors, and *Ccl20*+ microfold cells. To examine the absorptive enterocyte clusters in more detail, top-, mid-, and bottom-villus enterocytes were annotated based on zonation marker genes (*Ada* and *Neat1* for top-villus enterocytes, *Slc5a1* and *Slc2a2* for mid-villus enterocytes, and *Krt19* for bottom-villus enterocytes).[49] We annotated clusters 1, 4, 10, 12, and 15 as mid/top-villus enterocytes, as these clusters were not enriched for any known markers when compared to the rest of clusters, but were enriched for mid-villus enterocyte markers (*Slc5a1*, *Slc2a2*) when compared to the top-villus enterocytes (clusters 0 and 3), and for top-villus enterocyte markers (*Ada*, *Neat1*) when compared to either mid- (clusters 2, 5, 7, 8, and 16) or bottom-villus (clusters 6, 9, 17) enterocytes. See Table S3 for the full marker list.

Pseudobulk differential expression analysis

Given that differential expression (DE) analysis in scRNAseq uses cell as an independent replicate, this will lead to a large number of false positives between experimental conditions.[86] For this reason, we performed pseudobulk (DE) analysis using the DESeq2 package v1.40.2[71] to identify differentially expressed genes between conditions in each cluster. We generated pseudobulk replicates for each group by aggregating gene counts across the single cells to the sample level, then used DESeq2 to perform the DE analysis between conditions (virgin vs. lactating or control vs. knockout), considering mouse as an independent replicate.

Gene ontology enrichment analysis

Gene ontology (GO) enrichment analysis was performed using the clusterProfiler R package v4.8.3.[72,73] Genes with a FDR < 0.05 were used as DE genes. The gene-concept network plot was visualised using the cnetplot function from the enrichplot R package v1.20.3 (https://bioconductor.org/packages/release/bioc/html/enrichplot.html).

Xenium *in situ* spatial imaging analysis

FFPE tissues were analysed on the 10x Xenium Analyser instrument following 10X Genomics Xenium in situ Gene Expression protocols CG000580, CG000582 and CG000584. Briefly, 5 μm FFPE tissue sections were placed on Xenium slides, followed by deparaffinization and permeabilization to make the mRNA accessible. The standalone custom probes for 300 genes (Table S4) were hybridised for 20 hours overnight, followed by washing, ligation of the probe ends to the targeted RNAs generating circular DNA probes with high specificity. Rolling Circle Amplification was then used to generate hundreds of copies of the gene-specific barcode for each RNA binding event, resulting in a strong signal-to-noise ratio. Background fluorescence was then quenched chemically to mitigate tissue auto-fluorescence. The tissues sections were then stained with DAPI nuclear stain, and the Xenium slides were loaded onto the Xenium instrument for imaging and decoding image data to transcripts (Xenium software version 1.8.2.1). Secondary analysis to segment cells and assign transcripts was directly performed on-instrument. Xenium Explorer was used to evaluate data output quality and visualise initial morphology images, transcripts localization at subcellular resolution, segmentation and clustering data.

Data was analysed using Seurat v5.1.0.[87] The analysis was performed both using count matrices derived from the multimodal segmentation and from nuclei segmentation. The results from these analyses were highly consistent, with analogous cell populations identified in both. Cells with 0 counts were filtered from further analysis. The merged raw count matrix was normalised using the Seurat v5.1.0 NormalizeData function. The dataset was subsampled to 500,000 cells using the Seurat v5.1.0 SketchData function to ensure representation of rare populations. PCA was performed on all 300 genes and the top 30 PCs were selected for downstream dimensionality reduction using the UMAP algorithm and subjected to Louvain clustering at resolution 0.3. Cluster markers were identified using a Wilcoxon test, comparing each cluster to the union of all other clusters. Identified cluster labels were projected onto the full dataset using the Seurat v5.1.0 ProjectData function. Epithelial clusters were identified based on the expression of known epithelial markers (Table S4) and by their co-localisation in reduced dimensions. Cells from these clusters were selected for further analysis. The sketched epithelial data was subjected to PCA (300 genes), dimensionality reduction using the UMAP algorithm and Louvain clustering at resolution 0.5 (30 PCs). Cluster markers were again identified using a Wilcoxon test, comparing each cluster to the union of all other clusters and cluster labels were projected onto the full dataset using the Seurat v5.1.0 ProjectData function. Of note, good mixing between samples from all slides can be seen on both the UMAP of the whole dataset and the epithelial UMAP, with no sample specific clusters observed, suggesting minimal batch effects. For all further analyses the full (rather than sketched) datasets were used. Cell segmentation, cluster assignments and morphology images were visualised using the python SpatialData framework.[88]

Epithelial cell types were annotated based on the expression of known marker genes[48] as well as marker analysis in our single-cell RNAseq dataset. Specifically, we annotated *Mki67*+ isthmus progenitors, *Lgr5*+*Ang4*+*Lyz1*+ CBCs/Paneth, *Clca1*+*Tff3*+*Agr2*+ goblet cells, Chga+Chgb+ enteroendocrine cells, *Neurog3*+*Neurod2*+ enteroendocrine progenitors, *Dclk1*+ tuft cells, *Ccl20*+ microfold cells, and *Wnt5a*+ telocytes. To examine the absorptive enterocyte clusters in more detail, top-, mid-, and bottom-villus enterocytes were annotated based on zonation marker genes (*Ada* and *Neat1* for top-villus, *Slc5a1* and *Slc2a2* for mid-villus, and *Car4* for bottom-villus clusters)[49] as well as their spatial localization within villi. See Table S4 for the full marker list.

A pseudobulk approach was used to identify differentially expressed genes between conditions (virgin, pregnant and lactating) for each cluster in a pairwise manner using DESeq2 v1.44.0, and the design formula ~slide + condition.

The propeller method, available in the speckle v1.4.0 package,[74] was used to test for differences in cell type proportions between conditions, using the design formula ~0 + condition + slide.

Cell areas were calculated from the multimodal cell segmentations generated by the Xenium platform. A linear mixed-effects model was constructed to test for differences in cell size between conditions, using the lmer function from the R package lme4 v1.1-28[75] and the formula ln(cell area) ~condition + (1 | slide/sample). Post-hoc tests were conducted using the R package emmeans v1.10.4.[89]

QUANTIFICATION AND STATISTICAL ANALYSIS

Imaging

Images were acquired as follows. IHC and H&E sections were scanned using an Axio Scan Z1 slide scanner (Zeiss); IF sections were scanned using a Stellaris 5 or SP5 II confocal microscope (Leica); RNAscope FISH sections were scanned using the Akoya PhenoImager HT (formerly Vectra Polaris) using MOTiF scanning mode. The same settings were applied to both experimental and control groups. Images were processed using Fiji (Image J)[90] and analysed using QuPath.[91]

Cell detection, classification, and measurement in IHC, IF, and FISH images were performed by using cell segmentation algorithms in QuPath.[92,93] For cell size quantification, H&E images of whole cross sections were used. Villus regions (excluding crypts and muscle layers) were manually segmented and automated cell detection was used to measure each cell area within the segmented area. To quantify the intensity of FISH signals within the cell, whole cross section or gut roll samples were used. For the whole cross sections, 2 independent sections per mouse were measured, which were then analysed as nested data in a linear-mixed effects model (lme4 and lmerTest R package). For the cell death analysis, the crypt, bottom and mid–villus, and top–villus regions in the whole cross sections were manually segmented. Cell death proportions were calculated by dividing DAB+ (CC3 or TUNEL) cells by total cells in each segmented region. Cell classification based on the FISH signal intensity was performed on the whole cross sections and gut roll sections. Differences in cell type proportions between conditions were tested using the propeller method (speckle v1.4.0 R package).[74]

Mucosal morphometric analysis

Histology was analysed using formalin-fixed, paraffin-embedded (FFPE) sections. Small intestinal pieces were fixed in 10% neutral buffered formalin for 24 h at room temperature, and were then transferred into 70% ethanol. Tissue was processed to paraffin blocks and 5 μm transverse sections cut using a rotary microtome. Sections were stained using standard haematoxylin and eosin (H&E) staining protocols. H&E sections were scanned using an Axio Scan Z1 slide scanner (Zeiss) with a 20x objective. We only used fully perpendicular sections which did not show truncated villi (indicative of an oblique cut). For each transverse section, villus height, villus width, and crypt depth were manually annotated using QuPath software.[91] Broken villi or crypts were not measured. In total, around 20 villi/crypts from 2 independent sections were measured per mouse, which were then analysed as nested data in a linear-mixed effects model (lme4 and lmerTest R package). Specifically, we used the lmer function to account for nested structure of data (multiple measurement from multiple sections per mouse) as below (the response variable, Measurement (e.g. villus height, villus width, or crypt depth etc.); the fixed-effects, Group (e.g. virgin vs. pregnant vs. lactating or control vs. knockout etc.); the random effects, Section, which is nested within Mouse).

$$> \text{fm1} <- \text{lmer}(\text{Measurement} \sim \text{Group} + (1|\text{Mouse}/\text{Section}), \text{data} = \text{dataframe})$$

$$> \text{summary}(\text{fm1})$$

Statistical analyses

Statistical tests are specified in the figure legends. Nested data (multiple measurements per object) were analysed using a linear mixed-effects model (lme4 v1.1.35 and lmerTest v3.1.3 R package). Independent experiments (batch) were pooled and analysed as random effects using a linear mixed-effects model (lme4 and lmerTest R package). Two-way analysis of variance (ANOVA), Dunnett's, Sidak's or Tukey's post-hoc tests, and were performed using GraphPad Prism v10.1.1 software (GraphPad Software). To test differences in the proportion of cell types or cell classifications between conditions, the propeller method (speckle v1.4.0 R package) was used.[74] For electrophysiology data, analysis was performed using Clampfit software (Molecular Devices). We consider a P value of 0.05 significant. Significance levels of $^{*}p < 0.05$, $^{**}p < 0.01$, $^{***}p < 0.001$ used throughout.

CellPress
OPEN ACCESS

Supplemental figures

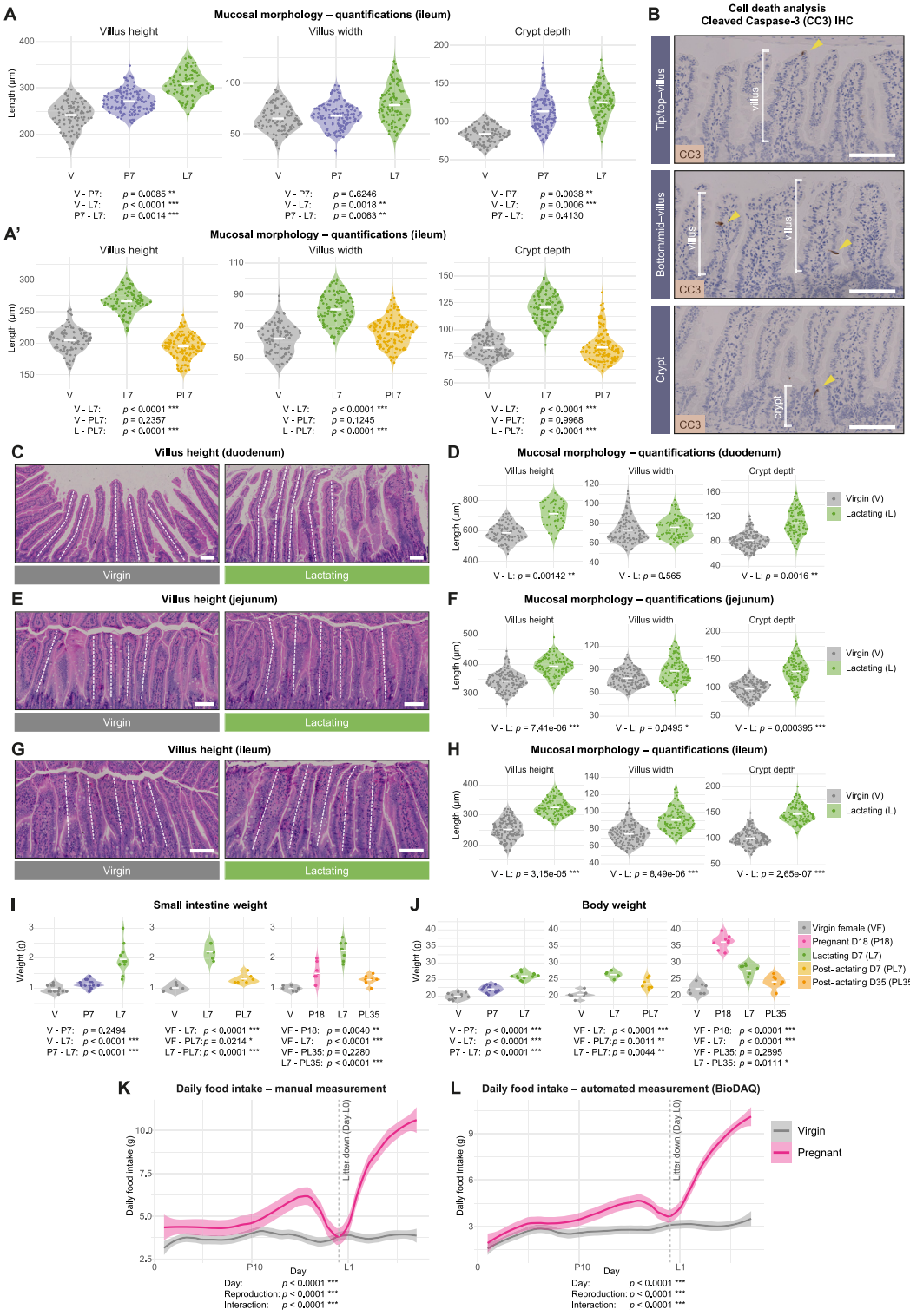

(legend on next page)

Figure S1. Regional profiling of dynamics and reversibility of villi growth during pregnancy, related to Figures 1 and 2

(A and A′) Morphometric quantifications of ileal villus height, villus width, and crypt depth of V ($n = 6$), P7 ($n = 9$), and L7 ($n = 7$) mice (A) and V ($n = 6$), L7 ($n = 6$), and PL7 ($n = 7$) mice (A′). Around 20 villi/crypts from 2 sections per mouse were measured, which was analyzed as nested data in a linear mixed-effects model.

(B) Representative images of anti-cleaved caspase-3 staining in the ileum (CC3-positive cells in tip/top-villus, bottom/mid villus, and crypt are shown in the top, mid, and bottom, respectively). Scale bars, 100 μm.

(C, E, and G) Representative H&E images of duodenum (C), jejunum (E), and ileum (G) of V, L (2^{nd} pregnancy) mice. Scale bars, 100 μm.

(D, F, and H) Morphometric quantifications of duodenal (D), jejunal (F), and ileal (H) villus height, villus width, and crypt depth of V ($n = 9$) and L (2^{nd} lactating, $n = 7$) mice. Around 15–20 villi/crypts from 2 independent sections were measured per mouse, which were then analyzed as nested data in a linear mixed-effects model.

(I and J) Small intestine weight (I) and body weight (J) of V ($n = 12$), P7 ($n = 15$), and L7 ($n = 12$) mice (left); V ($n = 6$), L7 ($n = 6$) and PL7 ($n = 7$) mice (center); and V ($n = 7$), P18 ($n = 8$), L7 ($n = 8$), and PL35 ($n = 7$) mice (right).

(K and L) Time course analysis of food intake in age- and experimentally matched V ($n = 5$ and 9), pregnant ($n = 6$ and 9), and lactating ($n = 9$ and 9) mice was determined by manual measurement (K) and the BioDAQ automated assay (L), respectively.

Original sections analyzed in (H) are also used in Figures 1F, 7B, and 7E (control). Original data used in (K) are also shown in Figures S3C and S3D.

p values are estimated using a linear mixed-effects model (lme4 and lmerTest R package; see STAR Methods for details) with a two-sample test in (A), (A′), (D), (F), and (H); a one-way ANOVA with Tukey's multiple comparisons test in (I) and (J); and a two-way ANOVA for repeated measurements with Sidak's multiple comparisons test in (K) and (L). In all quantifications, $*p < 0.05$, $**p < 0.01$, $***p < 0.001$.

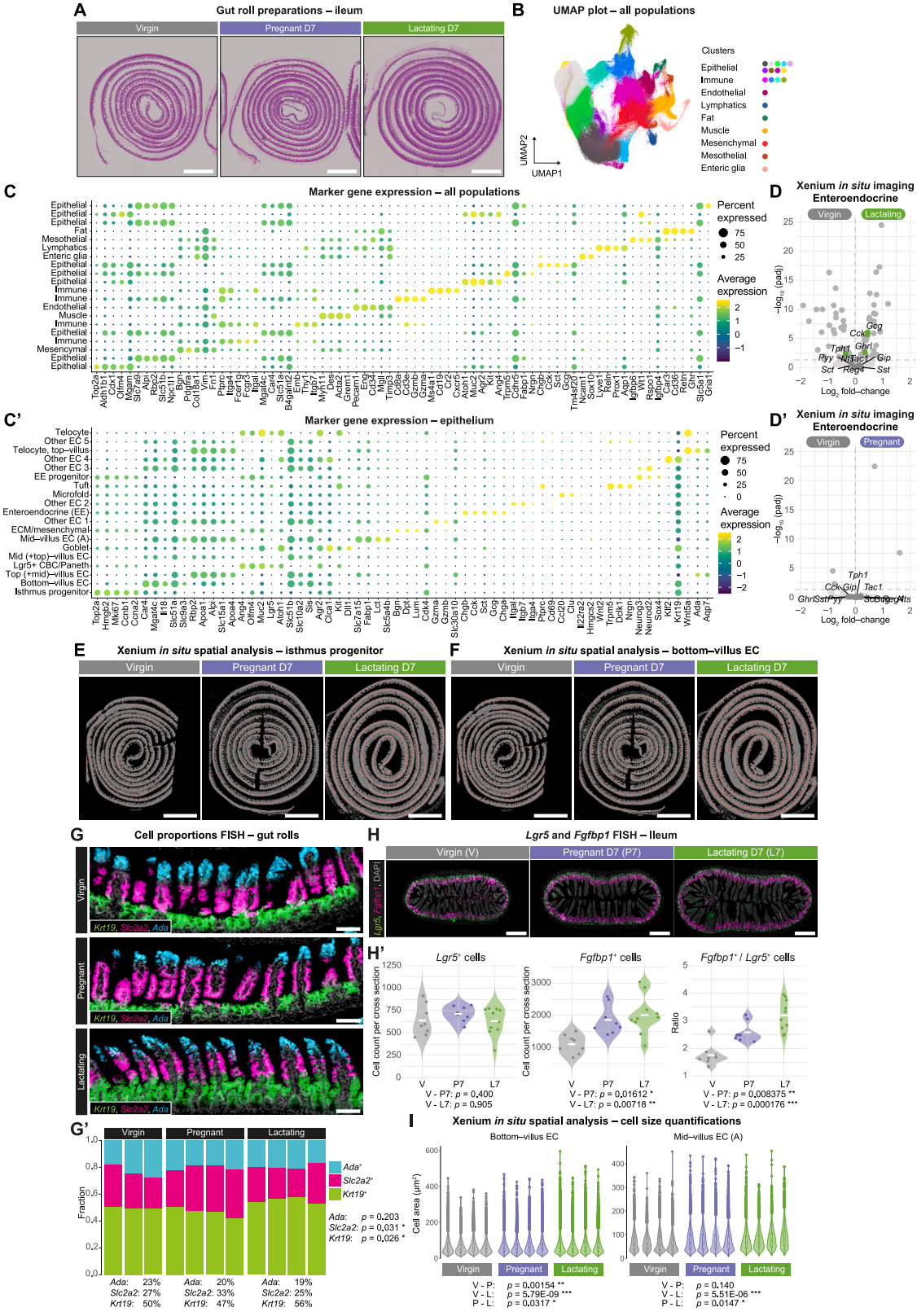

(legend on next page)

Figure S2. Transcriptional and spatial characterization of maternal gut remodeling during reproduction, related to Figure 4

(A) Representative H&E images of ileal gut roll preparation of V, P7, and L7 mice. Scale bars, 2,000 μm.

(B) UMAP visualization of unsupervised clustering of 3,410,861 cells from ileal gut rolls of V (n = 4), P7 (n = 4), and L7 (n = 4) mice.

(C and C′) Dot plots showing top 5 cell-type-enriched markers for each cluster in all populations (C) and epithelial subclusters (C′). The color scale represents the mean expression level; dot size represents the percentage of cells with non-zero expression within a given cluster. See Table S4 for the full marker list.

(D and D′) Volcano plots showing DE genes (FDR < 0.05, above the dotted horizontal line) between L and V (top) or P and V (bottom) in EE clusters in the Xenium *in situ* dataset. Genes coding for EE hormones are labeled; *Cck*, *Gcg*, and *Ghrl* are significantly upregulated during lactation.

(E and F) Representative images showing spatial localization of isthmus progenitor (E) and bottom-villus EC (F) in V, P7, and L7 mice. Scale bars, 2,000 μm.

(G and G′) Representative FISH images (*Krt19* in green, *Slc2a2* in magenta, and *Ada* in cyan) in ileal gut rolls of V (n = 3), P7 (n = 4), and L7 (n = 4) mice (G). Stacked bar plots showing cell proportions in each condition. The propeller method was used to test for differences in cell-type proportion between conditions (G′). Scale bars, 100 μm.

(H and H′) Representative FISH images (*Lgr5* in green; *Fgfbp1* in magenta) in ileal cross section of V (n = 5), P7 (n = 5), and L7 (n = 6) mice (H) and quantifications (H′). In each mouse, 2 independent cross sections were used for the measurement, which was analyzed as nested data in a linear mixed-effects model. Scale bars, 100 μm.

(I) Quantifications of cell size in ileal gut rolls of V (n = 4), P7 (n = 4), and L7 (n = 4) in bottom-villus EC (left) and mid-villus EC (right).

p values are estimated using a linear mixed-effects model (lme4 and lmerTest R package; see STAR Methods for details) with a two-sample test in (H′) and (I) and the propeller method (speckle R package; see STAR Methods for details) in (G′). In all quantifications, $^{*}p < 0.05$, $^{**}p < 0.01$, $^{***}p < 0.001$.

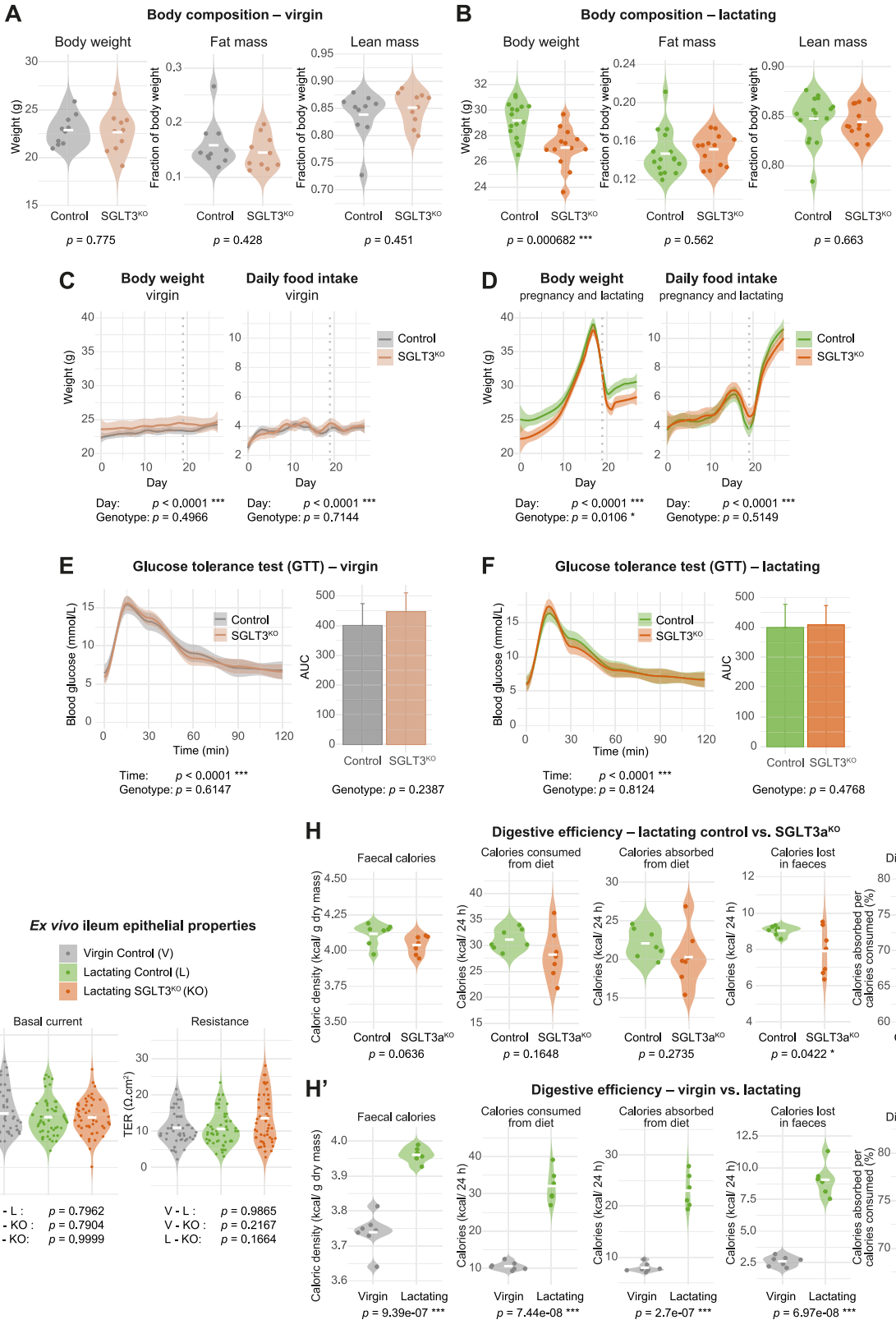

(legend on next page)

Figure S3. SGLT3 mutation does not impair broad digestive functions, related to Figure 5

(A and B) EchoMRI measurements of body weight, fat mass (fraction of body weight), and lean mass (fraction of body weight) in V (A) and L (B) control and SGLT3^{KO} female mice (V control, n = 10; V SGLT3^{KO}, n = 10; L control, n = 16; L SGLT3^{KO}, n = 13).

(C and D) Body weight and daily food intake of V (C) or L (D) control and SGLT3^{KO} female mice (V control, n = 5; V SGLT3^{KO}, n = 5; L control, n = 6–9; L SGLT3^{KO}, n = 6–7).

(E and F) Oral glucose tolerance test (OGTT) in V (E) and L (F) control vs. SGLT3^{KO} female mice (V control, n = 5; V SGLT3^{KO}, n = 5; L control, n = 6; L SGLT3^{KO}, n = 6). In both (E) and (F), blood glucose concentrations are displayed as a function of time (left) and as the cumulative area under the curve (AUC, right).

(G) Characterization of ileum epithelial properties, basal current (left), and resistance (right) in V control (n = 7), L control (n = 7), and SGLT3^{KO} (n = 7) mice determined by *ex vivo* Ussing chamber electrophysiology (see STAR Methods for details).

(H and H′) Quantifications of digestive efficiency in L control (n = 7) and SGLT3a^{KO} (n = 7) mice (H) and V (n = 7) and L (n = 6) (H′). Fecal caloric density was determined by bomb calorimetry. Calories consumed from diet were calculated by multiplying caloric density of food and daily food intake. Calories lost in feces were calculated by multiplying caloric density of feces and daily feces amount. Calories absorbed from diet were calculated by subtracting calorie lost in feces from calorie consumed from diet. Digestive efficiency was calculated by dividing calories absorbed by calories consumed from diet.

p values are estimated using a linear mixed-effects model (lme4 and lmerTest R package; see STAR Methods for details) with a two-sample test in (A), (B), (G), (H) and (H′); a two-way ANOVA for repeated measurements in (C)–(F); and unpaired t test in (C) and (D) for AUC. In all quantifications, $^{*}p < 0.05$, $^{**}p < 0.01$, $^{***}p < 0.001$.

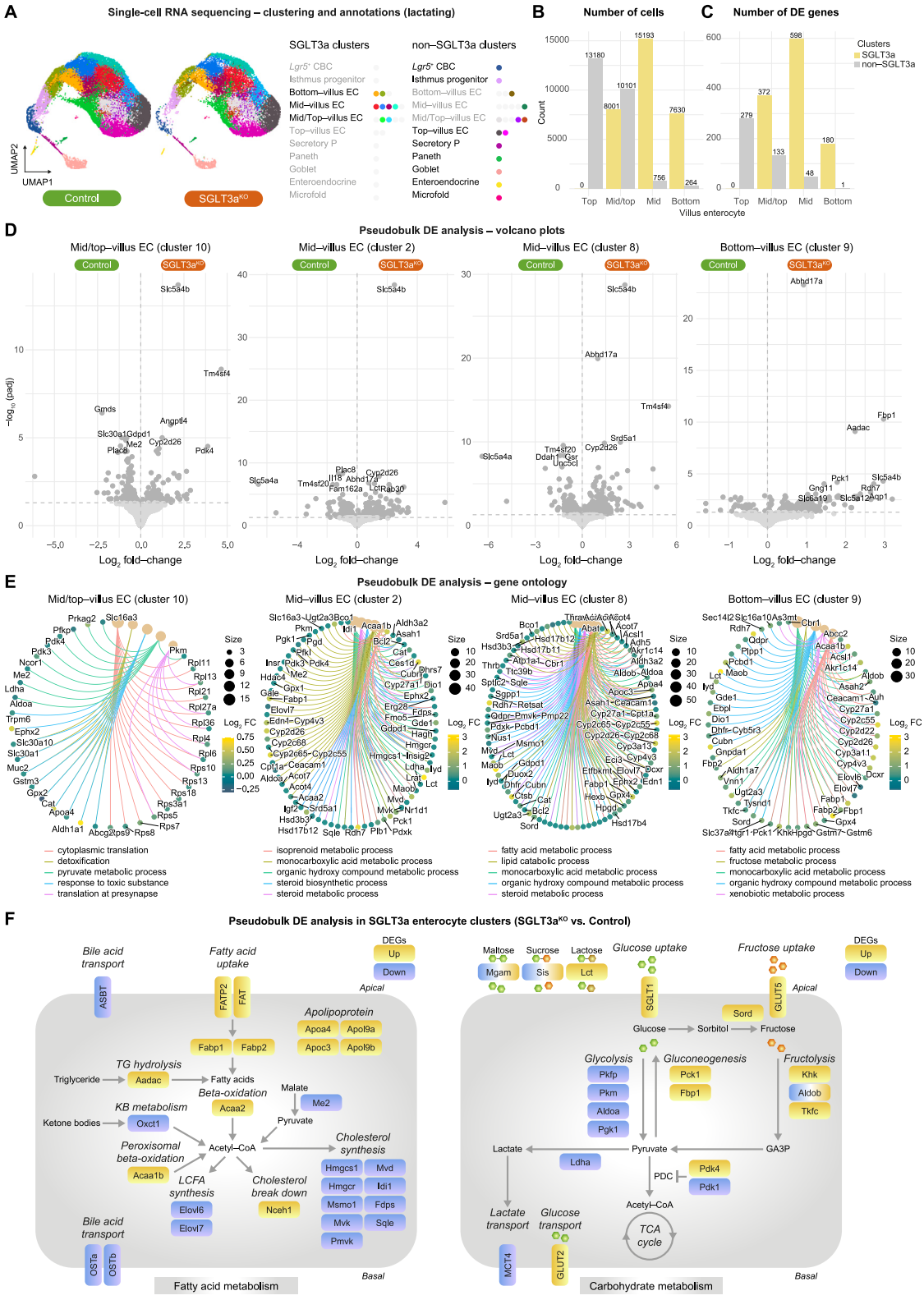

(legend on next page)

Figure S4. SGLT3a sustains metabolic plasticity within enterocytes, related to Figure 5

(A) UMAP visualization of unsupervised clustering of 22 distinct intestinal epithelial clusters identified in the ileum of lactating control (left, 39,958 cells from $n = 6$ mice) and SGLT3a^{KO} (right, 20,213 cells from $n = 3$ mice) samples. SGLT3a and non-SGLT3a clusters are also listed. CBC, crypt base columnar; EC, enterocyte; P, progenitor.

(B and C) Number of cells (B) and DE genes (C) in SGLT3a and non-SGLT3a enterocyte clusters.

(D) Volcano plots showing DE genes (FDR < 0.05, above the dotted horizontal line) between lactating SGLT3a^{KO} and control in SGLT3a clusters: mid/top-villus EC (cluster 10), mid-villus EC (clusters 2 and 8), and bottom-villus EC (cluster 9).

(E) Network plots of the top 5 enrichment terms for DE genes identified by pseudobulk DE analysis in SGLT3a clusters: mid/top-villus EC (cluster 10), mid-villus EC (clusters 2 and 8), and bottom-villus EC (cluster 9).

(F) Schematic showing fatty acid metabolism (left) and carbohydrate metabolism (right). Upregulation and downregulation of DE genes (FDR < 0.05, SGLT3a^{KO} vs. control in SGLT3a enterocyte clusters) in pseudobulk DE analysis are highlighted in yellow and blue, respectively. Genes upregulated in a cluster(s) and downregulated in another cluster(s) are highlighted in both yellow and blue.

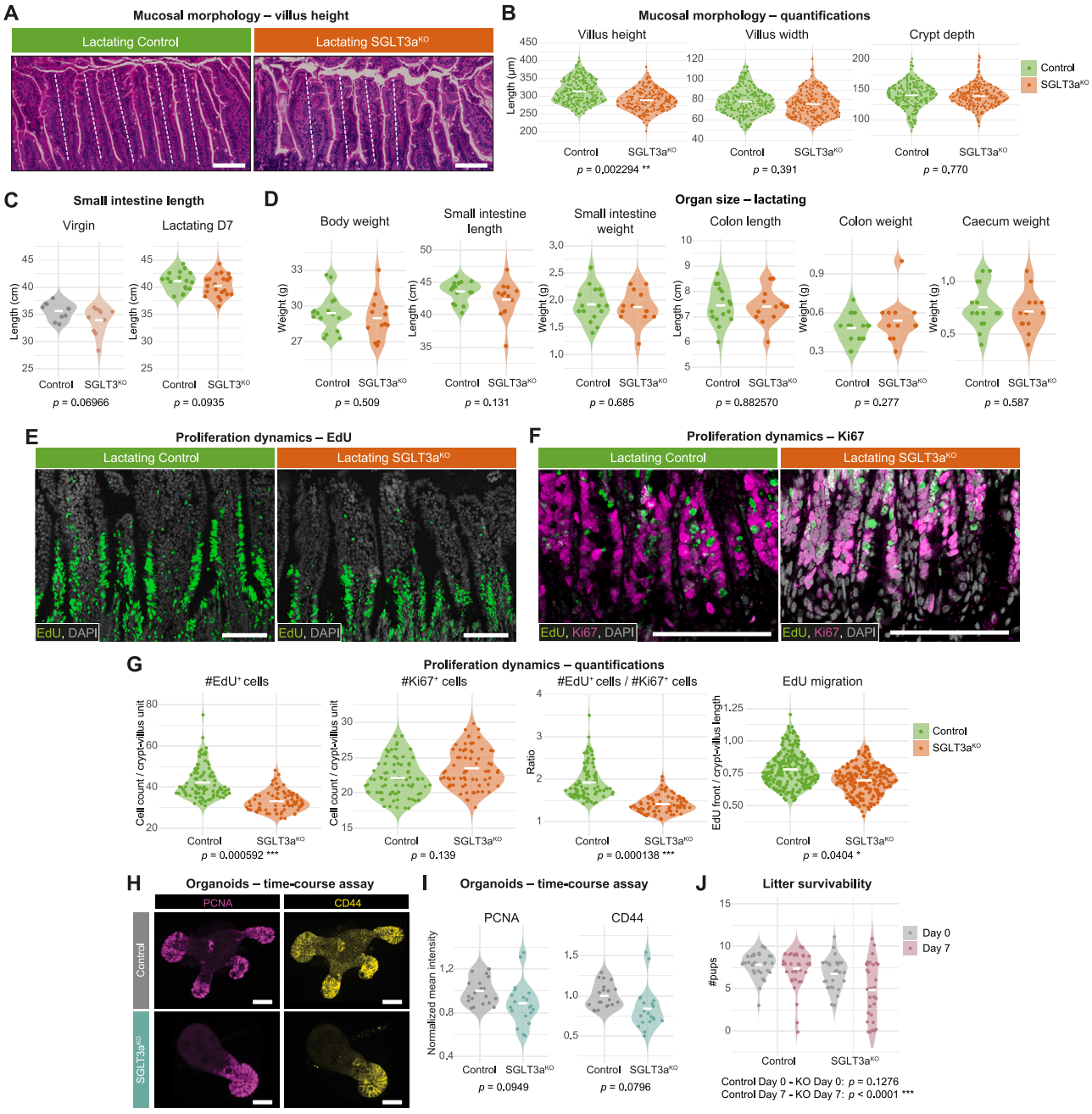

Figure S5. Enterocyte SGLT3a sustains the reproductive expansion of Fgfbp1 progenitors and promotes intestinal epithelial growth, related to Figure 7

(A) Representative H&E images of ileal villus height of lactating control and SGLT3a^{KO} mice. Scale bars, 100 µm.

(B) Morphometric quantifications of ileal villus height, villus width, and crypt depth in lactating control (n = 15) and SGLT3a^{KO} (n = 12) female mice. Around 20 villi/crypts from 2 sections per mouse were measured, which was analyzed as nested data in a mixed-effects model.

(C) Small intestine length of V and L mice in control or SGLT3^{KO} (V control, n = 10; V SGLT3^{KO}, n = 10; L control, n = 17; L SGLT3^{KO}, n = 21).

(D) Body weight and organ size of lactating control (n = 13) and SGLT3a^{KO} (n = 16) female mice.

(E and F) Representative IF images of EdU (E) and anti-Ki67 (F) stainings in the ileum of lactating control and SGLT3a^{KO} mice. EdU pulse was introduced by i.p. injection, and the gut tissues were harvested 24 h after injection. Scale bars, 100 µm.

(G) Quantifications of proliferation dynamics in the ileum of lactating control (n = 10) and SGLT3a^{KO} (n = 10) female mice. The ratio between the number of EdU+ cells and the average number of Ki67+ cells provides an indication of the proliferative capacity of progenitors. Migration distances are normalized by the reproductive changes in length by dividing the length of EdU coverage (from the base of the crypt to the highest point of the EdU staining in villi) by the average

(legend continued on next page)

crypt-villus length. Around 20 (migration) or 10 (cell counts) measurements were obtained per mouse, which were then analyzed as nested data in a linear mixed-effects model.

(H) Representative images of anti-PCNA (magenta) and CD44 (yellow) antibody staining for detecting crypt morphology. Scale bars, 50 μm.

(I) Quantifications of normalized intensity of PCNA (left) or CD44 (right) in organoids derived from control mice (n = 4 experiments, organoids derived from 3 different mice) or SGLT3a^{KO} mice (n = 4 experiments, organoids derived from 3 different mice).

(J) Litter size at lactation days 0 and 7 in control (n = 36 dams) or SGLT3a^{KO} (n = 30 dams) mice.

p values are estimated using a linear mixed-effects model (lme4 and lmerTest R package; see STAR Methods for details) with a two-sample test in (B)–(D), (G), and (I) and a two-way ANOVA with Sidak's multiple comparisons test in (J). In all quantifications, $^{*}p < 0.05$, $^{**}p < 0.01$, $^{***}p < 0.001$.

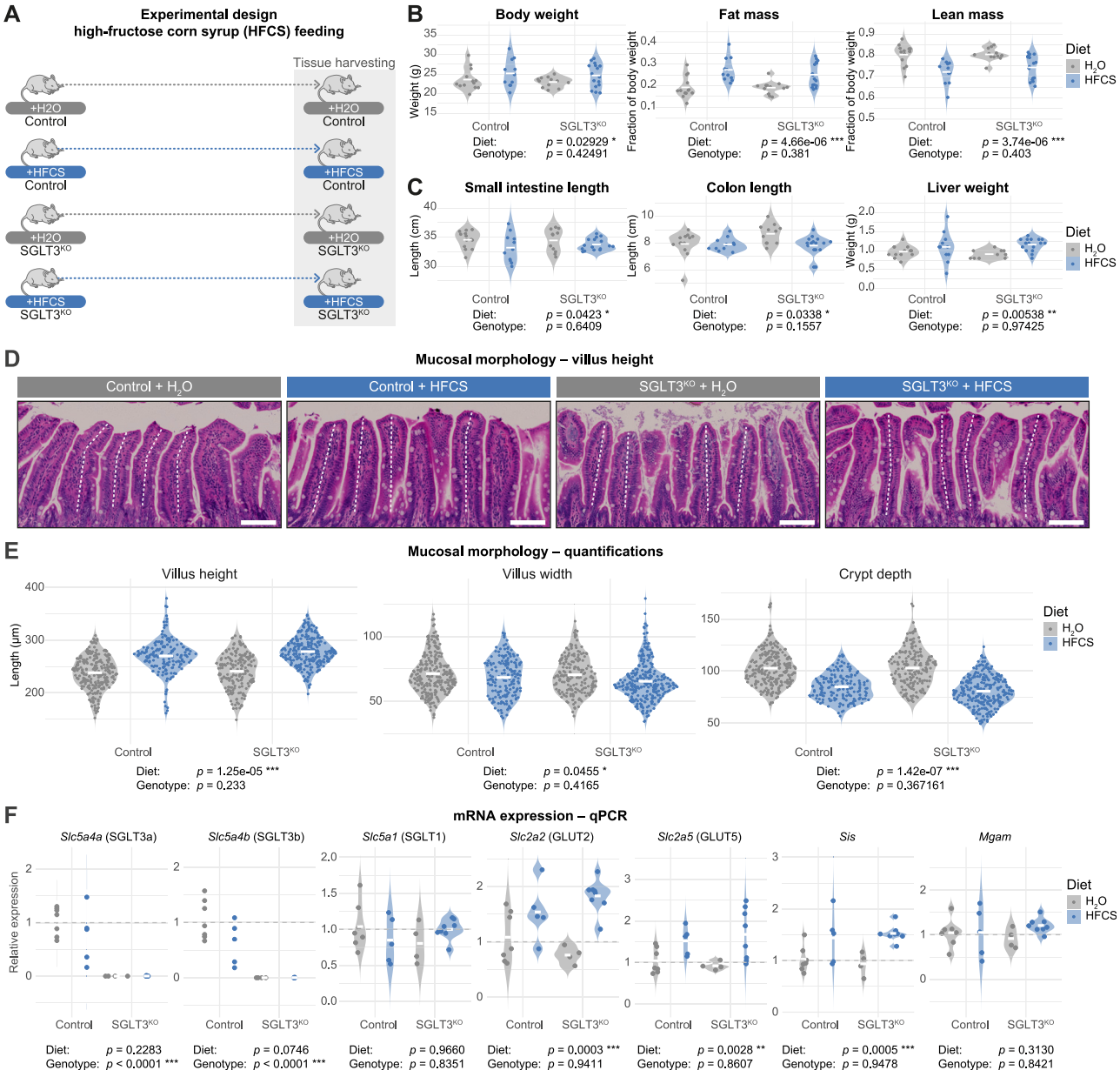

Figure S6. SGLT3 is not required for dietary-fructose-induced villus growth, related to Figure 7

(A) Summary of experimental design. Control and SGLT3^{KO} mice are fed a normal diet with *ad libitum* high-fructose corn syrup (HFCS) or H_2O control for 4 and 6 weeks for EchoMRI measurement and tissue harvesting, respectively (see STAR Methods for details).

(B) EchoMRI measurements of body weight, fat mass (fraction of body weight), and lean mass (fraction of body weight) in control and SGLT3^{KO} female mice fed a normal diet with *ad libitum* HFCS or H_2O control for 4 weeks (H_2O-fed control, n = 13; HFCS-fed control, n = 11; H_2O-fed SGLT3^{KO}, n = 12; HFCS-fed SGLT3^{KO}, n = 16).

(C) Small intestinal length, colon length, and liver weight of control and SGLT3^{KO} female mice fed an HFCS or H_2O control for 4 weeks (H_2O-fed control, n = 13; HFCS-fed control, n = 11; H_2O-fed SGLT3^{KO}, n = 11; HFCS-fed SGLT3^{KO}, n = 16).

(D) Representative H&E images of the ileum in control and SGLT3^{KO} female mice fed an HFCS or H_2O control for 6 weeks. Scale bars, 100 µm.

(E) Morphometric quantifications of ileal villus height, villus width, and crypt depth in control and SGLT3^{KO} female mice fed an HFCS or H_2O control for 6 weeks (H_2O-fed control, n = 13; HFCS-fed control, n = 11; H_2O-fed SGLT3^{KO}, n = 10; HFCS-fed SGLT3^{KO}, n = 15). Around 20 villi/crypts from 2 independent sections were measured per mouse, which were then analyzed as nested data in a linear mixed-effects model.

(F) Expression of genes coding for proteins with roles in carbohydrate uptake/metabolism in the ileum of control and SGLT3^{KO} female mice fed an HFCS or H_2O control for 6 weeks determined by RT-qPCR (H_2O-fed control, n = 7; HFCS-fed control, n = 5; H_2O-fed SGLT3^{KO}, n = 4; HFCS-fed SGLT3^{KO}, n = 8). *Sis*, sucrase isomaltase; *Mgam*, maltase-glucoamylase.

p values are estimated using a linear mixed-effects model (lme4 and lmerTest R package; see STAR Methods for details) with a two-sample test in (B), (C), and (E) and a two-way ANOVA in (F). In all quantifications, *p < 0.05, **p < 0.01, ***p < 0.001.

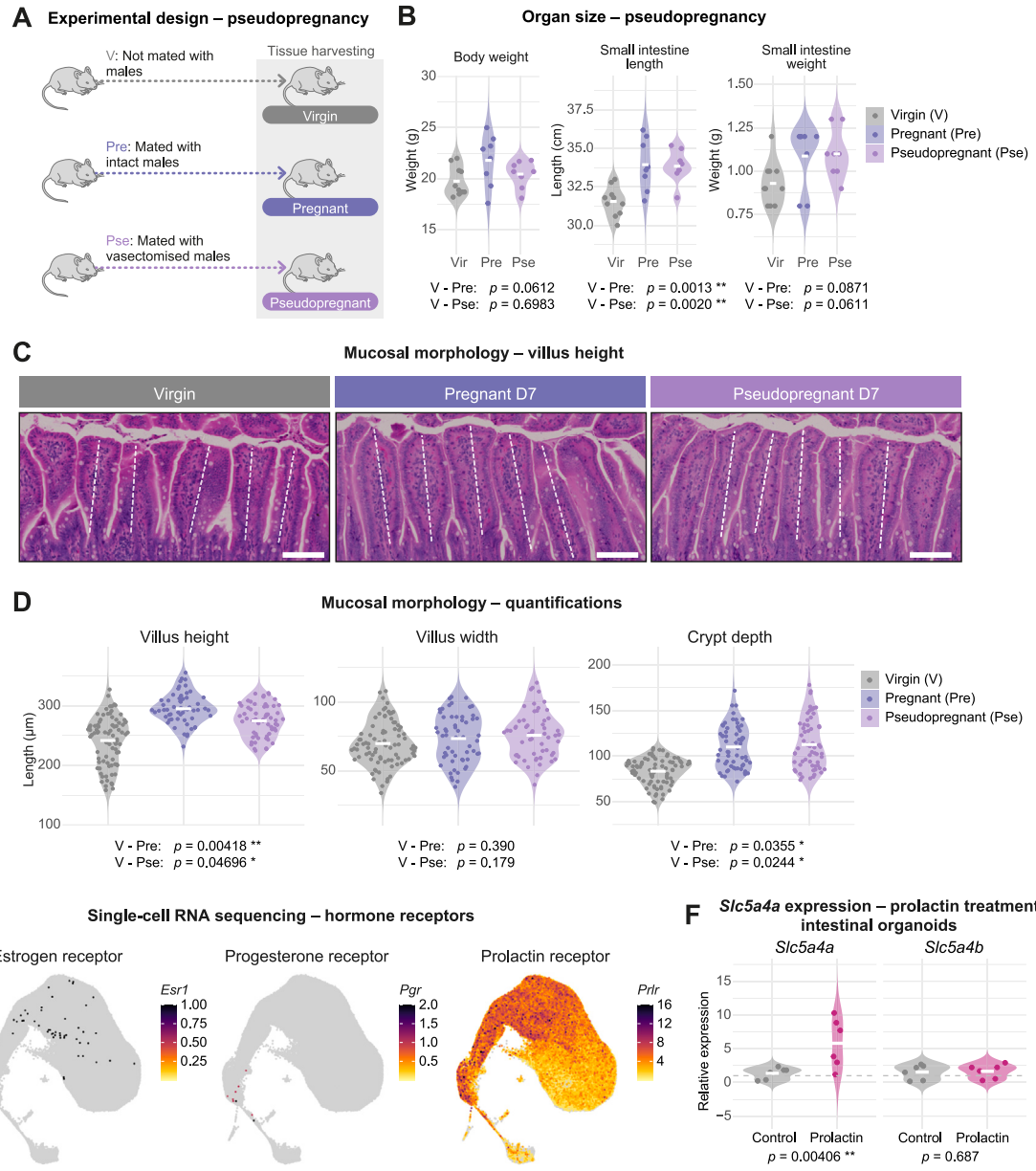

Figure S7. Effects of pseudopregnancy and reproductive hormones on maternal gut growth and SGLT3a induction, related to Figure 7

(A) Summary of experimental design. Pregnancy or pseudopregnancy was defined by detection of a vaginal plug after mating with intact or vasectomized males, respectively.

(B) Body weight, small intestinal length, and small intestine weight of V (n = 10), pregnant day 7 (Pre, n = 8), and pseudopregnant day 7 (Pse, n = 8) mice.

(C) Representative H&E images of ileal villus height of V, Pre, and Pse mice. Scale bars, 100 µm.

(D) Morphometric quantifications of ileal villus height, villus width, and crypt depth of V (n = 6), Pre (Pre, n = 5), and Pse (n = 5) mice. Around 12 villi/crypts per mouse were measured, which was analyzed as nested data in a linear mixed-effects model.

(E) Feature plots showing the expression of hormone receptors (*Esr1*, estrogen receptor; *Pgr*, progesterone receptor; *Prlr*, prolactin receptor) on the UMAP plot in our scRNA-seq dataset.

(F) Expression of *Slc5a4a* and *Slc5a4b* in organoids derived from ileum of control mice with or without prolactin treatment (n = 3) determined by RT-qPCR.

p values are estimated using a one-way ANOVA with Tukey's multiple comparisons test in (B) and a linear mixed-effects model (lme4 and lmerTest R package; see STAR Methods for details) with a two-sample test in (D) and (F). In all quantifications, $^{*}p < 0.05$, $^{**}p < 0.01$, $^{***}p < 0.001$.